

1 **Is there a discrepancy between geological and geodetic slip rates along the San**
2 **Andreas Fault System?**

3

4 Xiaopeng Tong, Bridget Smith-Konter, David T. Sandwell

5

6

7

8

Abstract

10 Previous inversions for slip rate along the San Andreas Fault
11 System (SAFS), based on elastic half-space models, show a
12 discrepancy between the geologic and geodetic slip rates along a
13 few major fault segments. In this study we use an earthquake cycle
14 model representing an elastic plate over viscoelastic half-space to
15 demonstrate that there is no significant discrepancy between long-
16 term geologic and geodetic slip rates. The model includes 41 major
17 fault segments having steady slip from the base of the locked zone
18 to the base of the elastic plate and episodic shallow slip based on
19 known historical ruptures and geologic recurrence intervals. The
20 slip rates are constrained by 1,981 secular velocity measurements
21 from GPS and L-band Interferometric Synthetic Aperture Radar
22 (InSAR). A model with a thick elastic plate (60 km) and half-space
23 viscosity of 10^{19} Pa·s is preferred because it produces
24 the smallest misfit to both the geologic and the geodetic data. We
25 find that the geodetic slip rates from the thick plate model agrees to
26 within the bounds of the geologic slip rates, while the rates from the
27 half-space model disagree on specific important fault segments such
28 as the Mojave and the North Coast segment of the San Andreas
29 fault. The plate models have generally higher slip rates than the
30 half-space model because most of the faults along the SAFS are late
31 in the earthquake cycle, so today they are moving slower than the
32 long-term cycle-averaged velocity as governed by the viscoelastic
33 relaxation process.
34

36 1 Introduction

37

38 Geodesy has become an increasingly important tool for recovering crustal strain rates
39 in tectonically active regions. In California, the high-accuracy GPS velocity field from
40 continuous and campaign networks, such as the Plate Boundary Observatory (PBO), and
41 Southern California Integrated GPS Network (SCIGN), and field surveys have been used
42 to estimate fault slip rates along the San Andreas Fault System (SAFS) [McCaffrey, 2005;
43 Meade and Hager, 2005; Bird, 2009; Zeng and Shen, 2010], especially for those faults
44 where geological estimation is lacking or inaccurate. The long term fault slip rates on
45 these major faults are an important component in earthquake hazard analysis because one
46 can estimate moment accumulation rate when combined with estimates of the
47 seismogenic depth.

48 The common approach for inverting for fault slip rates is through application of
49 elastic half-space models [e.g. McCaffrey, 2005]. An important assumption in the half-
50 space model is that the observed velocity field is steady over time and the transient
51 effects from past earthquakes can be neglected. This assumption is valid if the relaxation
52 times of the lower lithosphere are much larger than half of the recurrence interval of a
53 given fault [e.g. Meade and Hager, 2005]. When this model applies to 3-dimensional
54 problems, the interseismic velocity field can be explained by a combination of rigid block
55 rotation with kinematically consistent fault slip rates and fault locking within the
56 interseismic period.

57 Recent studies [e.g. Bird, 2009; Zeng and Shen, 2010] suggest an apparent
58 discrepancy between the geologic and geodetic slip rates along the SAFS, although the
59 uncertainties resulting from both of these estimates are quite large. The fault segments
60 that are currently in debate include: the Imperial fault [Dawson and Weldon, 2013] the
61 southernmost San Andreas fault and the San Jancinto fault [Van der Woerd et al., 2006;
62 Lundgren et al., 2009; Lindsey and Fialko, 2013], the San Bernardino segment [Loveless
63 and Meade, 2011; Spinler et al., 2011; McGill et al., 2013], the Mojave segment [Savage
64 and Lisowski, 1998; Chuang and Johnson, 2011], the Eastern California Shear Zone
65 [Oskin et al., 2008], the creeping section [Titus et al., 2006; Toke et al., 2011], and the
66 Peninsular segment of the San Andreas fault [Geist and Andrews, 2000; McCaffrey,
67 2005].

68 The discrepancy can be possibly resolved by introducing viscoelastic relaxation [Nur
69 and Mavko, 1974; Savage and Prescott, 1978] to the interseismic velocity modeling. It
70 has been observed that following large earthquakes, the steady state motion is perturbed
71 by the viscoelastic response: the surface strain rate will increase immediately following
72 an event and diffuses away slowly over years or decades. The 1906 San Francisco
73 earthquake and the 1857 Fort Tejon earthquake may have had a long lasting postseismic
74 effect depending on the rheological properties of the lithosphere [Savage and Lisowski,
75 1998; Pollitz et al., 2004; Chuang and Johnson, 2011]. A range of viscosity structures
76 have been estimated from postseismic deformation following recent $M > 7$ earthquakes
77 [Pollitz et al., 2001; Kenner and Segall, 2003; Freed and Bürgmann., 2004; Smith and
78 Sandwell, 2004].

79 The goal of this study is to estimate fault slip rates using both the viscoelastic
80 coupling model and the elastic half-space model to answer the following questions: How
81 do the fault slip rates inferred using geodesy compare to the geological estimates? Along

82 which fault segment of the SAFS are the geodetic and geologic slip rates are
83 incompatible? Can these discrepancies be reconciled by the viscoelastic earthquake cycle
84 model?

85 In order to answer the above questions, we incorporate GPS velocity data, InSAR
86 line-of-sight (LOS) velocity data and geological data to construct a high resolution
87 deformation model of the SAFS, starting from the Cerro Prieto fault to the south to the
88 Maacama fault to the north (Figure 1). We simultaneously solve for the long-term fault
89 slip rates of 41 major faults using a 3-dimensional earthquake cycle model. Then we
90 focus on key faults where discrepancies between the geodetic and geologic slip rates are
91 significant.

92

93 **2 Data**

94 **2.1 GPS velocities**

95 The GPS data used in this study include 1,981 horizontal velocity vectors covering
96 major faults along the SAFS (Figure 2). 1,863 velocity vectors were used from the SCEC
97 UCERF3 GPS velocity solutions [Herring, 2013, *personal communication*]. These
98 measurements are a blend of eight different analyses including the Plate Boundary
99 Observatory (PBO) GPS sites and continuous and campaign GPS sites from the SCEC
100 Crust Motion Model (CMM4) [Shen *et al.*, 2011] and the Measures solutions [Herring,
101 2013, *personal communication*].

102 When modeling the interseismic velocity field, it is important to keep in mind how the
103 GPS solutions are derived and what they represent. The GPS velocities span the years
104 from 1996 to present. Secular velocity terms are estimated, along with any postseismic
105 signals (logarithmic functions) for the events after 1996. The postseismic signals from
106 earthquakes before 1996, like the 1992 Landers earthquake, 1906 San Francisco
107 earthquake, and 1857 Fort Tejon earthquake are not accounted for in the GPS data
108 analysis [Herring, 2013, *personal communication*]. In this study, we correct the secular
109 velocity field solution for postseismic relaxation following the 1992 Landers earthquake
110 using a slip model from Fialko [2004]. Our model predicts that the postseismic velocity
111 after approximately 20 years of the Landers earthquake is ~ 1.5 mm/yr at maximum for
112 the sites surrounding the rupture. This corrected secular velocity field is used in the slip
113 rate inversion. The postseismic relaxation from the 1906 and 1857 events and other past
114 earthquakes are treated systematically in our earthquake cycle model (Section 3).

115 In addition, we added velocities from 8 campaign sites in Central California
116 [Rolandone *et al.*, 2008] that cover the central portion of the creeping section. A new
117 velocity field from 110 campaign sites near Salton Trough in Southern California
118 [Crowell *et al.*, 2013] were also included to provide a dense coverage of the near-fault
119 deformation near the Imperial fault. Both of the campaign GPS results were rotated into
120 the reference frame of the continuous GPS sites to yield a consistent velocity field.
121 Because these GPS solutions are different in terms of observation duration, uncertainties,
122 and processing technique, we quantify their importance by assigning a weighting factor
123 to the different data sets. The weight to the PBO data set from T. Herring is 1. The weight
124 to the campaign data set from Rolandone *et al.* [2008] and Crowell *et al.* [2013] is 0.5

125 and 0.33, respectively, because of relatively short observation periods of each. We focus
126 on the horizontal GPS velocity data only; no vertical velocities are used in this study.

127

128 **2.2 InSAR LOS velocities**

129 The InSAR data used in this study were obtained through an L-band radar onboard
130 Advanced Land Observing Satellite (ALOS) launched by Japanese Space and
131 Exploration Agency (JAXA), which can maintain good temporal coherence in vegetated
132 areas compared to C-band radar. The InSAR data (spanning 4.5 years from 2006.5 to
133 2011) were acquired along the ascending orbits (351° flight direction in azimuth with 34°
134 look angle). The InSAR LOS velocities (Figure 2) are derived from integration of the
135 radar interferogram stacking and GPS velocities [Tong *et al.*, 2013]. In this previous
136 study, the long wavelength of the velocity field (>40 km) was constrained by GPS and
137 InSAR and was used to retrieve the short wavelength (<40 km) features of the
138 deformation spectrum. A detailed description of the integration method can be found in
139 Tong *et al.* [2013]. The main contribution of the InSAR data is to recover details of the
140 aseismic fault creep on the creeping section and the faults of the northern SAFS.

141 For aspects of this study, we first made a mask for the InSAR LOS velocity data to
142 isolate non-tectonic effects. We identified 47 anomalous areas that exhibit anthropogenic-
143 related ground motion, most likely caused by groundwater extraction, along the major
144 faults in California. These anomalous areas are evident because they produce large
145 vertical motion either confined by known aquifers or bounded by faults. The data within
146 these anomalous areas were not used. The remaining LOS velocity data were down
147 sampled to 53,792 points based on the second invariant of the strain rates. This
148 subsampled dataset provides full resolution in high velocity gradient area near the faults
149 and lower resolution in areas of low strain rate far away from the faults. The 3-
150 component look vectors and the standard deviations for each LOS velocity data point
151 were subsampled in the same manner. The uncertainties of the LOS velocities are larger
152 than GPS measurements, typically 3-4 mm/yr. Data accuracy would be greatly improved
153 if the InSAR mission had a longer duration and if a second LOS direction along
154 descending orbits were available. The ALOS-2 mission, scheduled for launch at the
155 beginning of 2014, could provide two look directions (ascending and descending) so
156 future data will likely resolve these issues.

157 **2.3 Geological data**

158 The fault slip rates of closely-spaced parallel faults such as the Elsinore, San Jacinto,
159 and San Andreas in Southern California and the San Andreas, Maacama, and Green
160 Valley faults in Northern California are difficult to resolve using geodesy alone. To make
161 a kinematically consistent model, we introduced three types of geological conditions to
162 loosely constrain the fault slip rates. First, we attempted to constrain the recovered slip
163 rate to be within the upper and lower bounds of the quaternary fault slip rates. The
164 quaternary fault slip rates used in this study are from the Working Group on California
165 Earthquake Probabilities (WGCEP) [Dawson and Weldon, 2013]. We assigned each
166 estimate an uncertainty to account for the variability in quaternary fault slip rate derived
167 by different investigators compiled in Appendix B in UCERF3 (Table 1). Second, we
168 introduced a closure criterion at fault branching points such that when two fault strands

169 join into a single strand, the sum of the two strand rates should match the single strand
170 rate. This condition has an analog to the classic triple junction closure criteria at plate
171 intersections, except that all the faults in this case are approximately parallel to each
172 other. Third, we required that the sum of slip rates on parallel strands should
173 approximately match the overall relative slip rate along the plate boundary (e.g., ~45
174 mm/yr).

175 In order to make a fair comparison between the recovered geodetic slip rates and the
176 geological estimates, we treated the geological constraint with caution. The best approach
177 we found was to apply a weighting parameter in the inversion to quantify the significance
178 of the geological constraints. The best-fit weight for the geological constraints was found
179 through a grid search (see Section 4 for details). In fact, this approach can be deemed as
180 conservative because the recovered geodetic slip rates are required to match the geologic
181 slip rates in the inversion. Thus the difference between the geologic and geodetic slip rate
182 results is more likely to be caused by real discrepancy instead of non-uniqueness inherent
183 in the inversion.

184

185 **3 Earthquake cycle model**

186 To calculate surface velocities from locked faults, we used a fully 3-dimensional,
187 time-dependent earthquake cycle model [*Savage and Prescott, 1978; Smith and Sandwell,*
188 *2006*]. The model comprises an elastic plate overlying a viscoelastic half-space (here we
189 refer to it as the “plate model” in contrast to the “half-space model”). The earthquake
190 cycle effect produces time-dependent deformation by viscoelastic relaxation of the
191 asthenosphere. This model assumes a linear rheology of the viscous layer corresponding
192 to diffusion creep in the laboratory derived flow law.

193 Figure 3 shows an example of the surface interseismic velocity predicted by our
194 earthquake cycle model [*Smith and Sandwell, 2006*]. The difference between this model
195 and the elastic model are temporal variations of the present-day surface velocity. When
196 the observation time is earlier than the relaxation (or Maxwell) time, which is defined as
197 twice the effective viscosity divided by the shear modulus, the velocity is generally
198 higher than the cycle average (gray line), while for later times (when the observation time
199 is significantly later than the Maxwell time), the velocity is generally lower than the cycle
200 average. This comparison serves as a validation of our 3-dimensional forward model
201 against the 2-dimensional (2D) analytic solutions from *Savage and Prescott [1978]*.
202 What deviates from the original 2D model is that we incorporated realistic curved faults
203 in our 3-dimensional (3D) model and we use appropriate earthquake sequences based on
204 geologic records. Compared to the 2D model, the 3D model predicts a reduced
205 viscoelastic effect. Viscoelastic relaxation is proportional to the length of the fault
206 segment thus only significant earthquakes produce long lasting transient deformation.
207 This model is different from the traditional block models that use the “back-slip”
208 approach [*McCaffrey, 2005; Meade and Hager, 2005; Chuang and Johnson, 2011*] in that
209 this model describes faults as buried dislocations along block boundaries, i.e. “forward
210 slip”, to account for the interseismic locking effect [*Smith and Sandwell, 2006*].

211 In this model, the right lateral shear between the North American and Pacific plates is
212 taken up by several major strike-slip faults (Figure 1). In the long term, the crust is
213 displaced at the fault boundaries, behaving like rigid blocks. We restrict our analysis to

214 the simple fault geometry adopted from *Smith-Konter and Sandwell* [2009]. The modeled
215 faults include the entire trace of the San Andreas faults from Point Arena to Bombay
216 Beach: the San Jacinto fault, Elsinore fault, Imperial fault, and Cerro Prieto fault in
217 Southern California; the Hayward fault, Calaveras fault, Rodgers Creek fault, Maacama
218 fault, Hunting Creek - Bartlett Springs fault, and Concord fault in Central and Northern
219 California. In East California Shear Zone, we consider the Lenwood - Lockhart - Old
220 Woman Springs fault, Helendale fault, and Calico-Hidalgo fault. We also include the
221 Owens Valley fault and Death Valley fault with an aim to balance the slip budget across
222 the plate boundary.

223 In summary, the fault model consists of 41 fault segments, each having uniform slip
224 rate, locking depth, and earthquake history. Each segment is further sub-divided into
225 smaller patches (~ 5 km length) following the curvature of the fault trace at surface. Each
226 fault segment slips at a steady velocity from its locking depth to the base of the elastic
227 plate. The coseismic rupture is assumed to extend from the surface to the locking depth
228 prescribed for each fault segment. The locking depth of each fault is estimated by the
229 seismogenic depth and GPS observations [*Smith-Konter et al.*, 2011].

230 Our experiment explores four different rheological models: an elastic half-space model
231 and three elastic plate models (Table 2). We use two possible thicknesses (thick versus
232 thin plate) for the elastic plate in an attempt to understand the behavior of the viscoelastic
233 relaxation in relation to the lithosphere's rheology. The half-space model has localized
234 slip from the locking depth to infinite depth. In contrast, the plate models have localized
235 slip from the locking depth extending to the base of the elastic layer. This localized slip
236 surface approximates a deep-rooted shear zone beneath the fault zone in the upper crust.
237 An important difference between the plate model and half-space model is that the elastic
238 strain in the interior of the plate is much greater than the elastic strain in the interior of
239 the half-space blocks.

240 We note that the earthquake recurrence along many fault segments of the SAF is
241 irregular based on the paleoseismological record. Oversimplification of the earthquake
242 sequence using a characteristic earthquake model may not be appropriate. We used
243 realistic earthquake sequences based on a recent compilation of all the historical and
244 prehistorical earthquakes dated from the year 1000 to present [*Smith and Sandwell*, 2006
245 and references therein; *Solis*, 2013] to “spin up” the earthquake cycle. When the
246 information on the past earthquake sequences are lacking, we prescribed periodic
247 earthquake cycles according to the estimated recurrence interval [*Dawson and Weldon*,
248 2013]. Because the magnitude of the slip along each segment for each event is usually not
249 known, we assume that the shallow slip events “catch up” with the deep slip over an
250 earthquake cycle to satisfy block motion on the fault. This earthquake recurrence concept
251 is directly derived from the slip-predictable model. In Section 6.1 we investigate the
252 effect of this slip-predictable assumption in detail.

253 The deep-dislocation based earthquake cycle model cannot accurately resolve the
254 surface velocity due to aseismic creep in the upper crust. It is generally thought that the
255 fault creep is confined within the shallowest sedimentary layer of the crust (1 or 2 km
256 depth). However, it has been found that fault creep can occur within the brittle upper
257 crust along several major faults in Central and Northern California [*Rolandone et al.*,
258 2007]. We augmented this model using shallow dislocations in an elastic half-space
259 [*Wang et al.*, 2003]. The creeping faults modeled in this study include the Hayward,

260 Calaveras, Maacama, Concord, Bartlett Springs, Rodgers Creek fault, Parkfield, the
 261 creeping segment, and Santa Cruz Mountain segment of the San Andreas fault of the
 262 Northern SAFS and the Imperial, Superstition Hills, and the Brawley Seismic Zone of the
 263 Southern SAFS [Tong *et al.*, 2012]. These fault segments are discretized into small
 264 rectangular dislocation patches extending from the surface to 12 km deep in the upper
 265 crust. We jointly solved for the aseismic creep rates of these fault segments along with 41
 266 long term fault slip rates in the inversion as described in the next section. The details of
 267 the aseismic creeping faults in central and northern SAFS are out of the scope of this
 268 paper. These results are summarized in a companion paper [Tong *et al.*, manuscript in
 269 preparation].
 270

271 4 Inversion method

272 In this section, we describe the system of linear equations used to estimate slip rates
 273 on 41 fault segments \bar{s} and 66 creep rates \bar{p} from a combination of 1,981 GPS vector
 274 velocity measurements \bar{v}_g , 53,792 line-of-sight (LOS) InSAR measurements \bar{l} and
 275 geologic constraints. This linear system consists of four subsystems of equations
 276 representing the GPS data, InSAR data, geological constraints and smoothing constraints,
 277 respectively:

278

279

$$280 \begin{bmatrix} \bar{G}_g & \bar{E}_g & \bar{I} & \bar{r} \\ \bar{G}_i & \bar{E}_i & \bar{I} & \bar{r} \\ \bar{C} & 0 & 0 & 0 \\ 0 & \bar{S} & 0 & 0 \end{bmatrix} \begin{bmatrix} \bar{s} \\ \bar{p} \\ \bar{v}_0 \\ \bar{w} \end{bmatrix} = \begin{bmatrix} \bar{v}_g \\ \bar{l} \\ \bar{s}_c \\ 0 \end{bmatrix} \quad (1)$$

281

282 where \bar{G} and \bar{E} are the Green's function for modeled surface velocity. The subscripts g
 283 and i refer to GPS and InSAR data, respectively. \bar{G} is derived from the earthquake cycle
 284 model and it depends on the elastic plate thickness, effective viscosity, locking depth of
 285 the fault, and the earthquake sequence of the segment. \bar{E} is derived from the dislocation
 286 model depending on the elastic property of the material. \bar{C} is the constraint matrix, which
 287 includes the geologic slip rate estimates, the triple junction closure constraint, and the far-
 288 field velocity constraint. \bar{S} is the smoothing matrix applied only to the shallow
 289 dislocations representing the aseismic creep. In order to separate the effect of the plate
 290 rotation from the interseismic signal, we introduce \bar{v}_0 and \bar{w} representing the translation
 291 term and the rotation term of the velocity field in a cartesian coordinate. \bar{v}_0 has two
 292 unknowns denoting two translation terms in the east and north velocities. \bar{w} describes the
 293 rotation rate (one unknown) around a prescribed rotation axis that is orthogonal to the
 294 east and north velocity direction. \bar{r} represents the location of the velocity measurements
 295 with respect to the rotation axis. We do not intend to solve for the location of the rotation

296 axis and the rotation rate simultaneously because of the strong trade-offs between these
 297 two quantities. \bar{I} is the identify matrix. After running the inversion we found that the
 298 rotation term \bar{w} can absorb the residuals of the observed velocity field although it is
 299 relatively small in this particular tectonic setting.

300 In the second subsystem that incorporates InSAR data, variable look vectors in the east
 301 and north component are used to project the horizontal velocity into radar line-of-sight
 302 direction even though they are not shown explicitly in equation (1). The third subsystem
 303 $\bar{C}s = \bar{s}_c$ represents three types of geological constraints represented by the following
 304 three matrix: \bar{I} , \bar{C}_{tot} and \bar{C}_{tri} , respectively. 1) Matrix \bar{I} denotes the estimates of slip rate
 305 from the geologic data on 41 segments \bar{s}_{geol} . 2) Matrix \bar{C}_{tot} represents the constraint that
 306 the sum of slip rate on sub-parallel fault strands must equal the total slip rate across the
 307 plate boundary ($\bar{s}_{tot} = 45$ mm/yr). 3) Matrix \bar{C}_{tri} represents the constraint that at the fault
 308 junctions where two or more sub-parallel faults connect and converge into one main fault,
 309 the slip rate on the main fault must equal to the sum of the sub-parallel faults ($\bar{s}_{tri} = 0$).
 310 We can represent this as:

311

$$312 \begin{bmatrix} \bar{I} \\ \bar{C}_{tot} \\ \bar{C}_{tri} \end{bmatrix} s = \begin{bmatrix} \bar{s}_{geol} \\ \bar{s}_{tot} \\ \bar{s}_{tri} \end{bmatrix} \quad (2)$$

313

314 Equation (1) was normalized by the uncertainty in each component of the geodetic
 315 measurement. In addition, we introduced three weighting constants to the four sub-
 316 systems of equations to have a sense of control on the slip rates solutions. The relative
 317 weights were determined by a grid search method to minimize the RMS misfit of the
 318 GPS and InSAR data (Figure 4). The best-fit weighting parameter is set to ensure that the
 319 inversion gives the smallest misfit to the geodetic data.

320 We added Gaussian random noise to the input data and repeated the inversions 10
 321 times. Then we computed the mean and the standard deviations as the final fault slip rate
 322 results. The amplitude of the random noise was chosen according to the uncertainties of
 323 the geodetic measurements. Like other studies [McCaffrey, 2005] we modified the formal
 324 uncertainties of the GPS data to have more realistic slip rate uncertainty estimates from
 325 the inversion. The minimum uncertainties of the GPS velocity measurements are set to be
 326 1 mm/yr.

327 5 Results

328

329 5.1 The quality of fit

330 Table 2 shows the statistics of the misfits for four different models: an elastic half-
 331 space (HS) model, a viscoelastic model with a relatively thick elastic plate (60 km) and

332 moderate viscosity of 10^{19} Pa \cdot s (PL6019), a viscoelastic model with a thin elastic
 333 plate (30 km) and moderate viscosity of 10^{19} Pa \cdot s (PL3019), and a viscoelastic model
 334 with thin elastic plate (30 km) and relatively high viscosity 10^{20} Pa \cdot s (PL3020). The
 335 χ^2 misfit is defined as the squared sum of the residuals normalized by the standard
 336 deviation for each velocity measurement $\chi^2 = \frac{1}{N} \sum_{i=1}^N \left(\frac{o_i - m_i}{\sigma_i} \right)^2$ where o_i is the data, m_i is
 337 the model, and σ_i is the uncertainties for N measurements. The χ^2 misfit to the GPS
 338 data is 2.67 for HS, 2.56 for PL6019, 2.74 for PL3019, and 2.68 for PL3020 model. The
 339 formal uncertainties of the InSAR data are relatively large, thus the χ^2 misfit to InSAR
 340 are approximately 0.27.

341
 342 Figure 5a shows the 1,981 GPS velocity vectors and the predicted velocity from
 343 model PL6019. Our model is able to reproduce the right-lateral shear motion across the
 344 Pacific-North American plate boundary from the Cerro Prieto fault to the south to the
 345 Maacama fault to the north. The model captures the pronounced westward rotation of the
 346 velocity field along the Big Bend and Mojave segment of the SAFS in large scale. Figure
 347 5b shows the residual GPS velocity field for the same model PL6019. For illustrative
 348 purposes, only significant residuals that are greater than two times of the standard
 349 deviations are shown. There are residuals along the southern tip of the creeping section
 350 and the Mojave desert, which could be due to complicated postseismic signals from
 351 recent earthquakes. The residuals near the Channel Islands to the west of the California
 352 coast are probably caused by off-shore faults not included in our model. In general, we
 353 found that the secular velocity field observed by GPS is explained well by this 3-
 354 dimensional earthquake cycle model.

355 Figure 6 shows 53,792 InSAR LOS velocity point measurements, the prediction and
 356 its residuals from model PL6019 (Table 2). The InSAR observations added in the
 357 inversion provides improved resolution of the near-fault (<10 km from the fault trace)
 358 deformation. Our model can reproduce both the broad-scale deformation and the sharp
 359 velocity gradients at the creeping faults in California.

360

361 In addition we calculated the weighted RMS defined as $WRMS = \sqrt{\frac{\sum_{i=1}^N \left(\frac{o_i - m_i}{\sigma_i} \right)^2}{\sum_{i=1}^N \frac{1}{\sigma_i^2}}}$. The

362 weighted RMS residual to the GPS data are found to be 1.71 mm/yr for HS, 1.68 mm/yr
 363 for PL6019, 1.73 mm/yr for PL3019, 1.72 mm/yr for PL3020 model. The weighted RMS
 364 residuals to the InSAR data are less sensitive to different models: 1.34 mm/yr for HS,
 365 1.30 mm/yr for PL6019, 1.31 mm/yr for PL3019, and 1.34 mm/yr for PL3020. We found
 366 that the PL6019 model produces the smallest misfit to both of the GPS and InSAR data.
 367 The PL6019 model is marginally superior in matching observations to the PL3019 and
 368 PL3020 models, which indicates that the elastic thickness of the lithosphere underneath
 369 the SAFS is relatively thick. Different viscosities have minor influence on the model
 370 residuals.

371 In summary, the four models that we tested all yield satisfactory fit to the geodetic
372 observations. We can see that the above statistics of the quality of fit is not adequate to
373 differentiate the plate models from the half-space model. In Section 5.2, we investigate
374 the half-space and plate models using profiles of the GPS velocity measurements. In
375 Section 5.3 we compare the geodetic slip rates from the four models to the geologic slip
376 rates to identify statistically significant mismatches.
377

378 **5.2 GPS velocity profiles**

379

380 Figures 7a and 7b show 16 fault-perpendicular profiles of the GPS velocities at
381 different locations along the SAFS. These velocity profiles are plotted against the
382 velocities predicted by the half-space model (HS), a thick plate model (PL6019) and a
383 thin plate model (PL3019). We decomposed GPS velocities into two components,
384 parallel and perpendicular to the plate motion, using an Euler pole (-74.4° W, 50.1° N).
385 This pole is determined based on the pole of rotation analysis from *Wdowinski et al.*
386 [2007]. The parallel components, (shown as triangles) are compared to the modeled
387 velocities (colored solid lines). We selected those GPS sites that lie within 10 km of the
388 northern and southern sides of the profile. We have also tried to include more GPS sites
389 by enlarging the width of the profiles, but this increases the scatterness of the GPS
390 velocities. Since the 3D model has along-strike variation and the differences among the
391 three models are subtle, we decided to limit the width of our profiles to be 20 km. We
392 computed a weighted RMS misfit for each profile for each model with an aim of
393 differentiating the plate models from the half-space model and to explore spatial
394 variations of the plate thickness of the SAFS.

395 For profile (a) that crosses the Brawley seismic zone to the south of the Salton Sea in
396 Southern California, the thin plate model yields the best fit to the GPS data at a RMS of
397 2.85 mm/yr. Our fault geometry is based on the seismicity location in the crust even
398 though there is no evidence of surface breaks of an active fault. The model fit to the
399 velocities is good to the west of the Brawley seismic zone but gets worse to the east. The
400 Coachella segment of the San Andreas fault and the San Jancinto fault (profile b) is fit
401 within an RMS of ~ 1.4 mm/yr for all the three models. Profiles (c) and (d) suggest that
402 over the San Bernardino Mountain region, the geodetic data favor the thick plate model.
403 The residuals 100 km to the east of the SAF are likely due to unmodeled postseismic
404 signals from either the Landers or the Hector Mine earthquakes. The GPS velocities are
405 matched well by the half-space model (RMS=1.56 mm/yr) and the thick plate model
406 (RMS=1.61 mm/yr) at the Mojave segment (profile e), while the thin plate model gives a
407 misfit of 1.77 mm/yr, slightly worse than the other models. At the northern tip of the
408 Mojave segment (profile f), the difference in the plate thickness becomes more evident;
409 the RMS misfit of the thin plate model is 0.2 mm/yr greater than the thick plate model. It
410 is worth noting that approximately 50 km on either side from the SAF the thin plate
411 model predicts slower velocities than what is observed by GPS. GPS observations
412 provide evidence for the existence of a relatively thick (>60 km) plate underneath the
413 Mojave segment. Profile (g) crossing the central section of the Cholame-Carrizo segment
414 of the SAF reflects a strong asymmetry of the GPS velocities. We tested an alternative
415 fault geometry and discuss the results of this in Section 6.3. For profile (h), there is no
416 longer an asymmetry in GPS velocities.

417 For profile (i) (Figure 7b) that transects the locked portion of the Parkfield segment,
418 we infer that the thin plate model fits the GPS observations best with an RMS of 1.82
419 mm/yr. It suggests the existence of anomalous lithospheric structure underneath Parkfield.
420 From profile (j) it seems that the half-space model more appropriately represents the
421 creeping section and no earthquake cycle model is needed at the central portion of the
422 creeping section to explain the present-day GPS velocities. For the profile (k) that crosses
423 the Santa Cruz mountain, there are two closely spaced paralleling creeping faults, the San
424 Anreas fault and the Calaveras fault. They are well resolved by our model because of the
425 constraints provided by InSAR. The thick plate model provides the best fit (RMS = 1.34
426 mm/yr). The GPS data are fit almost perfectly at profile (l) crossing the southern portion
427 of the Pennisular segment of the SAF. The two steps in the velocity are due to surface
428 creep of the Hayward and Calaveras fault. At the north portion of the Pennisular segment
429 (profile m), the thick plate model produces the best fit (RMS = 1.51 mm/yr), compared to
430 1.68 mm/yr RMS from the half-space model and 1.61 mm/yr RMS from the thin plate. At
431 profile (n) that crosses the North Coast segment and the Rodgers Creek fault, the half-
432 space model predicts significant larger misfit than the plate models (RMS = 1.77mm/yr
433 versus 1.6 mm/yr). Surface creep is recovered along the Rodgers Creek fault and the
434 Hunting Creek fault.

435 Among all the profiles, the last two profiles (o and p) crossing the North Coast and
436 the Maacama fault are the most intriguing ones. Due to lack of constraints, the three
437 models we tested predict drastically different secular velocities. Our models deduce
438 significant aseismic creep on both of the Maacama and the Bartlett Springs fault. There is
439 little shear motion within the crustal block between the Maacama and Bartlett Springs
440 fault as constrained by the four GPS sites (between distance 425 km to 475 km) in profile
441 (o). To the north however, profile (p) reveals uniform shear within the same block. From
442 profile (p), the RMS misfit is smallest, favoring the thick plate model (2.06 mm/yr).
443 These models should be re-evaluated when more accurate geodetic data is available.

444 In summary, an analysis of the 16 GPS velocity profiles and the earthquake cycle
445 models across the entire SAFS suggests that the thick plate (60 km) is a more appropriate
446 representation in California, with exceptions at three important locations: the Brawley
447 seismic zone, the Parkfield segment and the creeping section. The modeling favors a
448 relatively thin (30 km) elastic plate near the Brawley seismic zone and the Parkfield
449 segment. The half-space model is preferred over the earthquake cycle models over the
450 center portion of the creeping section of the SAF. This section is known to be devoid of
451 large historical earthquakes and the plate motion is mainly accomodated by aseismic
452 creep.

453

454 **5.3 Long-term slip rate**

455 Here we compare the geodetic slip rates estimated from the inversion with geologic
456 slip rates. We incorporated the best estimate rates, as well as the upper and lower bounds,
457 derived from a recent compilation of the UCERF3 geologic slip rates [*Dawson and*
458 *Weldon, 2013*]. The geodetic slip rates inferred from the half-space model and four plate
459 models are shown separately (Figure 8). First, we evaluated a general misfit between the
460 geodetic slip rates and the best estimate geologic rates. These are: HS (3.5 mm/yr),
461 PL6019 (3.4 mm/yr), PL3019 (5.3 mm/yr) and PL3020 (4.0 mm/yr). From these results

462 we infer that agreement between geology and geodesy is better for the thick plate model
463 and the HS model.

464 Next, we focus our attention on fault segments where there are significant
465 discrepancies between the the geodetic slip rates for the half-space model and the
466 geologic rates. From Figure 8a and Table 1, we show that the HS model provides a
467 reasonably good job of matching the geologic rates. However, there are two interesting
468 anomalies: (1) the North Coast segment of the SAF is slipping at 14 mm/yr, much slower
469 than the preferred geologic rates at 24 mm/yr, and (2) the Mojave segment of the SAF is
470 slipping at 25 mm/yr while the geologic best estimate is 34 mm/yr with rather large
471 uncertainties (25-40 mm/yr).

472 We next examined the slip rates inferred from the plate models (also incorporating a
473 variable viscosity) to see if these differences could be explained. From Figure 8b and 8c,
474 we conclude that the earthquake cycle model could, in general, resolve the discrepancy
475 between the geodetic and geologic slip rates for both the Mojave segment and the North
476 Coast segment of the SAF. The thick plate model (PL6019) yielded a slip rate of 23
477 mm/yr on the North Coast segment, and a slip rate of 27.8 mm/yr of the Mojave segment.
478 The thin plate model (PL3019) resulted in a higher slip rate 36.5 mm/yr along the North
479 Coast segment and 33.1 mm/yr along the Mojave segment. It can be seen that the plate
480 thickness plays a key role in the recovered geodetic slip rate. For the North Coast
481 segment, the thick plate model is the best in terms of matching the geologic slip rates, but
482 for the Mojave segment, the thin plate model is the best. The effects of the viscosity on
483 the recovered slip rates can be interpreted by comparing Figure 8c and 8d. For the
484 Mojave segment, for example, increasing the mantle viscosity from 10^{19} Pa \cdot s to
485 10^{20} Pa \cdot s results in a dramatic decrease in the geodetic slip rates from 33.1 to 22.9
486 mm/yr. Similarly, for the North Coast segment, the viscosity change resulted in a
487 reduction in the slip rate estimation from 36.5 to 33.2 mm/yr.

488 Because of time-dependent viscoelastic relaxation effects, the interseismic velocity in
489 the early earthquake cycle is always faster than the cycle average [*Savage and Prescott,*
490 1978]. Likewise, the interseismic velocity in the late cycle is always slower than the cycle
491 average (Figure 3). The recovered slip rates for the plate models are strongly influenced
492 by the time at which the fault is in its earthquake cycle. The last event that occurred on
493 the North Coast segment of the SAFS was the 1906 San Francisco earthquake and the last
494 event on the Mojave segment was the 1857 Fort Tejon earthquake. Given a recurrence
495 interval of 200 years, both the Mojave section and the North Coast section of the SAF are
496 late in the earthquake cycle, so to fit the observed velocities, the model requires higher
497 fault slip rates. The earthquake cycle effect gets stronger as the elastic plate gets thinner.
498 The response time of the earthquake cycle effects are determined by the half-space
499 viscosity: a high viscosity implies a longer response time than a low viscosity.

500 We compared our results with recent findings by *Chuang and Johnson* [2011] and
501 *Hearn et al.* [2013]. Both of these detailed studies focused on the discrepancy along the
502 Mojave segment in Southern California. *Chuang and Johnson* [2011] estimated a slip
503 rates of 26 mm/yr along the Mojave segment assuming a three layer model. *Hearn et al.*
504 [2013] deduced the slip rates of the Mojave segment to be 27-29 mm/yr assuming a four
505 layer rheological model. Our results compared to these previous results shed new light on
506 the importance of the rheology in estimating the slip rate parameters. Because the elastic
507 plate thickness depends on the temporal characteristics of the loading, the elastic

508 thickness inferred from the earthquake cycles should be much greater than the ones
509 inferred from the isostatic rebound or gravity studies [Watts, 2007]. Using a plate model
510 and varying the elastic thickness of the plate, we demonstrated that the earthquake cycle
511 model could agree with the geologic slip rates of 34 mm/yr along the Mojave segment if
512 the elastic plate is relatively thin (30 km) and the half-space viscosity is 10^{19} Pa \cdot s .
513 The difficulty of accepting this solution is that the elastic plate underneath the Mojave
514 segment has to be unusually thin compared to the other regions of the SAFS. Another
515 possibility is that the geological slip rates of the Mojave segment is overestimated by
516 about 6 mm/yr.

517 We note that there are other anomalies between the half-space rates and the geologic
518 rates, which our earthquake cycles models cannot explain. The geodetic slip rates of the
519 Imperial fault and the Cerro Prieto fault are 10 mm/yr faster than the geologic estimates
520 of 35 mm/yr. The Lenwood - Lockhart - Old Woman Springs fault and Calico-Hidalgo
521 fault in the Mojave desert are also significantly faster than the geologic rates. The causes
522 of these inadequacies are probably due to poor knowledge about the fault structures and
523 the chronological sequence of the past events in those regions.

524 **6 Discussions**

525

526 **6.1 Past earthquakes assumption**

527

528 In this study, the timing of past events are derived from a compilation of historical and
529 prehistorical earthquake records [Smith and Sandwell, 2006 and reference therein]. We
530 assume that the coseismic slip of past events completely releases the slip deficit
531 accumulated since the last events. This assumption originated from the elastic rebound
532 theory which is probably correct over geological time scales. However, it is rather
533 difficult to collect a complete record of all the past earthquakes. There might be
534 significant deviations from a periodic behavior over a time span of several earthquake
535 cycles. For example, a study from Sieh *et al.* [2008] implied earthquake supercycles since
536 past 700 years at the Sumatra subduction zone.

537 Here we investigated the effect of past events on the geodetic slip rate using the
538 Mojave segment of the SAF. The Mojave segment has experienced the 1812
539 Wrightwood-Santa Barbara earthquake (M=7.5) and the 1857 Fort Tejon earthquake
540 (M7.9). Prehistorical earthquakes since the year 1000 A.D. are estimated to have occurred
541 around years 1016, 1116, 1264, 1360, 1487, 1536, and 1685. Under the slip predictable
542 model assumption, the slip magnitude of the 1812 event is three times greater than the
543 1857 event. Since the transient velocity from the postseismic relaxation is proportional to
544 the magnitude of the coseismic slip, the postseismic contribution following the 1857
545 rupture is three times smaller than the 1812 rupture.

546 We tested the influence of the 1857 rupture on present day velocities by considering
547 three scenarios: a) increasing the coseismic slip of the 1857 event by a factor of four; b)
548 removing the 1857 event from the earthquake sequence; c) adding a synthetic earthquake
549 in 1957 on this segment. The new slip rates of the Mojave segment are shown in Table 3.
550 Scenario a) and b) show that the 1857 event has little effects on the slip rate estimation
551 for a viscosity of 10^{19} Pa \cdot s . For a viscosity of 10^{20} Pa \cdot s , magnifying the 1857
552 postseismic signal by a factor of four can decrease the slip rate estimate by ~ 2 mm/yr;

553 removing the 1857 event can increase the slip rate estimate by ~ 1 mm/yr. Scenario c)
554 shows that the slip rate could be underestimated systematically, depending on viscosity, if
555 the timing of the last event is set to be later than its real occurrence.

556 We found that the influence of the slip-predictable hypothesis to the geodetic slip rates
557 is not significant, given a moderate viscosity of the substrate. However, it is important to
558 estimate the timing of the most recent events in order to determine whether the
559 earthquake cycle is in an early or late stage. It should be noted that the slip magnitude of
560 previous events is needed if one wants to evaluate the absolute magnitude of stress in the
561 lithosphere. *Hetland and Hager* [2006] considered such a model to investigate the
562 influence of the initial stress on the interseismic strain accumulation.

563 As pointed out by *Hearn et al.* [2013], the postseismic effect resulting from a single
564 earthquake is different from the long-lived transient effect resulted from multiple
565 earthquake cycles. For a finite length rupture in 3-dimensions, as considered in our
566 model, the postseismic effect is limited to a distance that is approximately the rupture
567 length. However, the cumulative earthquake cycle effect from all past events reaches
568 beyond the rupture length. This is because the viscoelastic relaxation effect is no longer
569 resultant from one particular fault segment but rather the contributions from all the other
570 fault segments in the region. This effect highlights the importance of incorporating
571 realistic past earthquake sequences into 3-dimensional earthquake cycle models.

572

573

574 **6.2 Spatial variations in elastic plate thickness inferred from secular GPS velocities**

575

576 For the plate models, the deformation beneath the elastic layer within the lower crust
577 and upper mantle is distributed by ductile flow. The viscosity of the lower crust/upper
578 mantle is found to be 9.5×10^{19} Pa \cdot s [*Kenner and Segall*, 2003] using post-1906
579 earthquake deformation data. Studies following earthquakes occurring in the Mojave
580 desert suggests time-dependent rheology consistent with power-law creep [*Pollitz et al.*,
581 2001; *Freed and Burgman*, 2004]. Because the rheological properties underneath
582 California are not known, we experimented with an effective viscosity of 10^{19} Pa \cdot s
583 and 10^{20} Pa \cdot s for the plate models. In earlier studies, *Hearn et al.* [2013] and *Chuang*
584 *and Johnson* [2011] has assumed different elastic layer thickness and a more
585 sophisticated viscosity structure representing lower crust, uppermost mantle and the
586 asthenosphere. *Chuang and Johnson* [2011]'s model consists of 20 km elastic plate, 10
587 km thick lower crust with a viscosity of 2×10^{20} Pa \cdot s and a half-space viscosity of $6 \times$
588 10^{18} Pa \cdot s. *Hearn et al.* [2013]'s model consists of 25 km elastic plate, 5 km thick
589 lower crust with a viscosity of 3×10^{19} Pa \cdot s, 20 km uppermost mantle with a
590 viscosity of 10^{21} Pa \cdot s and a half-space viscosity of 3×10^{18} Pa \cdot s. It is yet to be
591 determined whether the lower crust or the uppermost mantle has stronger viscous strength
592 in supporting the tectonic stress [*Bürgmann and Dresen*, 2008]. In this study, we do not
593 intend to differentiate the lower crust from the upper-most mantle; there are trade-offs
594 between the elastic thickness and the effective viscosity below [*Watts*, 2007], and in
595 general a thicker elastic plate implies higher viscosity in the lower crust and the upper
596 most mantle.

597 Along the SAFS where the fault geometry is simple, the effect of the plate thickness
598 on the internal elastic strain within the blocks is readily discernable (Figure 7a, profiles g

599 and h). The plate model produces prominent interseismic strain within internal elastic
600 blocks away from the fault in contrast to the half-space model. The amount of internal
601 elastic strain distributed within the block increases as the elastic plate thickness
602 decreases. This can be seen clearly that the thin plate model predicts significantly slower
603 secular velocities ~ 50 km away from the SAF than the thick-plate model. In the far-field,
604 at distances greater than ~ 100 km away from the fault, velocities inferred from the
605 aforementioned three models are essentially indistinguishable. We deduce the effective
606 elastic thickness to be 60 km over the Cholame-Carrizo segment.

607 Currently there is no consensus on the elastic plate thickness of California. Previous
608 studies using viscoelastic earthquake cycle models generally assume that the rheological
609 structure underneath California is uniform everywhere. *Smith and Sandwell* [2006]
610 deduced an overall elastic thickness of 70 km for the SAFS, in good agreement with 44-
611 100 km found by *Johnson and Segall* [2004]. In this study, we attempted to probe the
612 elastic thickness of the lithosphere using precise secular GPS velocity. By carefully
613 examining 16 GPS velocity profiles we infer that the elastic thickness is generally large
614 (~ 60 km) over most of the SAFS but is relatively small (~ 30 km) near the Brawley
615 Seismic Zone and the Parkfield. The anomalously thin elastic thickness implies low
616 effective viscosity in the lower crust/upper mantle, which can be caused by localized
617 thinning of the lithosphere due to high heat flux or presence of partial melt or fluid.

618

619

620

621 **6.3 Effect of dipping fault geometry**

622

623 From Figure 7a, the GPS velocity data along the central Carrizo segment appear
624 asymmetric across the SAF. It is possible that our slip rate inversion could be biased by
625 inaccurate representation of fault geometry. It has been proposed that the geometry of the
626 SAF is significantly different from vertical. In the southern SAF near the Coachella
627 valley, the fault is dipping towards the northeast [*Lindsey and Fialko*, 2013] and near the
628 “Big Bend” region the fault is dipping towards the southwest [*Fuis et al.*, 2012], where
629 the overall shape of the fault surface is similar to a “propeller”. The dipping geometry can
630 be further tested using the deformation models because a dipping fault will shift the
631 center of the strain concentration, which is observable in geodetic data. The gravity and
632 electromagnetic data suggest that the Carrizo segment maybe dipping to the west at 60
633 deg. We tested this dipping fault hypothesis using local GPS velocity data and the elastic
634 half-space model. The GPS data within 10 km from profile g shown in Figure 7a is used
635 in evaluating the model misfit. As shown in Figure 7a, the deformation model with the
636 SAF dipping to the west remarkably reduces the RMS misfit of the GPS data from 1.7
637 mm/yr to 0.96 mm/yr. This model comparison suggests that the dipping SAF hypothesis
638 is supported by the geodetic data. An alternative explanation of the asymmetric strain at
639 the Carrizo segment is through laterally varying crustal properties [*Schmalzle et al.*,
640 2006]. In their model, a weak zone with 10-25 km width to the northeast of the SAF is
641 required to explain the observed GPS velocity.

642 **7 Conclusions**

643

644 Since long-term slip rates estimated from geology are subject to uncertainties, present-
645 day geodetic measurements have been employed to estimate slip rates. We investigated
646 the geodetic slip rates of the SAFS using both a viscoelastic earthquake cycle model and
647 the elastic half-space model and compared them with geologic slip rates. Incorporating
648 1,981 GPS velocity vectors, 53,792 InSAR velocity points, and comprehensive
649 geological information into a constrained least-square problem, we examined 41 fault
650 segments along the SAFS to identify anomalous geodetic slip rates. We found that the
651 geodetic slip rates from an elastic half-space model are significantly lower than the
652 geologic estimates along the North Coast segment and the Mojave segment of the SAF by
653 about 10 mm/yr. This apparent discrepancy can be reconciled by introducing time-
654 dependent deformation governed by the viscoelastic earthquake cycle effect.

655 The influence of the earthquake cycle on geodetic slip rates depends strongly on the
656 rheologic structure of the lower crust and upper mantle. A 60 km thick elastic plate with
657 viscosity of 10^{19} Pa \cdot s provides the best fit to the geodetic and geological data. It is
658 observed that the earthquake cycle effect gets stronger as the elastic plate gets thinner.
659 For the Mojave segment the inferred slip rate is 27.8 mm/yr for the thick plate model and
660 is 33.1 mm/yr for the thin plate model. For the North Coast segment the inferred slip rate
661 is 23 mm/yr for the thick plate model, and is 36.5 mm/yr for the thin plate model. We
662 identified discrepancies on other faults along the SAFS such as the Imperial fault, the
663 Cerro Prieto fault and the faults in the East California Shear Zone (ECSZ), which cannot
664 be explained by the viscoelastic effect. Finally, we found that the influence of the slip-
665 predictable hypothesis to the recovered geodetic slip rates is not significant. This finding
666 implies that the present-day surface velocity measured by geodesy is not sensitive to the
667 magnitude of historical earthquakes hundreds of years ago.

668
669

670 **Reference**

671

672 Bird, P. (2009), Long-term fault slip rates, distributed deformation rates, and forecast of
673 seismicity in the western United States from joint fitting of community geologic,
674 geodetic, and stress direction data sets, *J. Geophys. Res.*, 114, B11403,
675 doi:10.1029/2009JB006317.

676

677 Bürgmann, R. and G. Dresen (2008), Rheology of the lower crust and upper mantle:
678 Evidence from rock mechanics, geodesy and field observations, *Ann. Rev. Earth Plan.*
679 *Sci.*, v. 36, p. 531-567, doi:10.1146/annurev.earth.36.031207.124326.

680

681 Chuang, R. Y. and K. M. Johnson (2011), Reconciling geologic and geodetic model fault
682 slip-rate discrepancies in Southern California: Consideration of nonsteady mantle flow
683 and lower crustal fault creep, *Geology*, 39(7), 627-630, doi:10.1130/G32120.32121.

684

685 Crowell, B.W (2013), Using GPS to Rapidly Detect and Model Earthquakes and
686 Transient Deformation Events, PhD thesis, Dept. of Geophys., Univ. of Calif. San Diego,
687 U.S.A.

688

689 Dawson, T.E. and R.J. Weldon II (2013), Appendix B: Geologic slip-rate data and
690 geologic deformation model, U.S. Geol. Surv., Menlo Park, California, U.S.A.

691

692 Fialko, Y. (2004). Probing the mechanical properties of seismically active crust with
693 space geodesy: Study of the coseismic deformation due to the 1992 Mw7. 3 Landers
694 (southern California) earthquake, *J. Geophys. Res.*, 109, B03307, doi:
695 10.1029/2003JB002756.

696

697 Freed, A. M. and R. Bürgmann (2004), Evidence of power-law flow in the Mojave desert
698 mantle, *Nature*, v. 430, p. 548-551., doi:10.1038/nature02784.

699

700 Fuis, G. S., D. S. Scheirer, V. E. Langenheim, and M. D. Kohler (2012), A new
701 perspective on the geometry of the San Andreas Fault in southern California and its
702 relationship to lithospheric structure, *Bulletin of the Seismological Society of America*,
703 102(1), 236–251.

704

705 Geist, E. L. and D. J. Andrews (2000), Slip rates on San Francisco Bay area faults from
706 anelastic deformation of the continental lithosphere. *J. Geophys. Res.*, 105(B11), 25543-
707 25552.

708

709 Hetland, E.A. and B. H. Hager (2006), Interseismic strain accumulation: Spin-up, cycle
710 invariance, and irregular rupture sequences, *Geochem. Geophys. Geosyst.*, 7, Q05004,
711 doi:10.1029/2005GC001087.

712

713 Hearn E. H., F. F. Pollitz, W. R. Thatcher, and C. T. Onishi (2013), How do “ghost
714 transients” from past earthquakes affect GPS slip rate estimates on southern California
715 faults?, *Geochem. Geophys. Geosyst.*, 14, 828–838, doi:10.1002/ggge.20080.

716
717 Johnson, K. M. and P. Segall (2004), Viscoelastic earthquake cycle models with deep
718 stress-driven creep along the San Andreas fault system. *J. Geophys. Res.*, 109(B10).
719
720 Kenner, S. J. and P. Segall (2003), Lower crustal structure in northern California:
721 Implications from strain rate variations following the 1906 San Francisco earthquake. *J.*
722 *Geophys. Res.*, 108(B1).
723
724 Lindsey, E. O. and Y. Fialko (2013), Geodetic slip rates in the southern San Andreas
725 Fault system: Effects of elastic heterogeneity and fault geometry. *J. Geophys. Res.*, 118,
726 689-697.
727
728 Loveless, J. P. and B.J. Meade (2011). Stress modulation on the San Andreas fault by
729 interseismic fault system interactions, *Geology*, 39(11), 1035-1038.
730
731 Lundgren, P., E. A. Hetland, Z. Liu, and E. J. Fielding (2009), Southern San Andreas-San
732 Jacinto fault system slip rates estimated from earthquake cycle models constrained by gps
733 and interferometric synthetic aperture radar observations, *J. Geophys. Res.*, 114, B02403,
734 doi:10.1029/2008JB005996.
735
736 McCaffrey, R. (2005), Block kinematics of the Pacific-North America plate boundary in
737 the southwestern United States from inversion of GPS, seismological, and geologic data,
738 *J. Geophys. Res.*, 110(B07401), doi: 10.1029/2004jb003307.
739
740 McGill, S. F., L. A. Owen, R. J. Weldon II, and K. J. Kendrick (2013), Latest Pleistocene
741 and Holocene slip rate for the San Bernardino strand of the San Andreas fault, Plunge
742 Creek, Southern California: Implications for strain partitioning within the southern San
743 Andreas fault system for the last ~35 k.y., *Geological Society of America Bulletin*, v.
744 125, no. 1-2, doi:10.1130/B30647.1.
745
746 Meade, B. J. and B. H. Hager (2005), Spatial localization of moment deficits in southern
747 California, *J. Geophys. Res.*, 110(B4), B04,402, 10.1029/2004JB003331.
748
749 Nur, A., and G. Mavko (1974), Postseismic viscoelastic rebound. *Science*, 183(4121),
750 204-206.
751
752 Oskin, M., L. Perg, E. Shelef, M. Strane, E. Gurney, B. Singer, and X. Zhang (2008),
753 Elevated shear zone loading rate during an earthquake cluster in eastern California,
754 *Geology*, 36, 507–510, doi:10.1130/G24814A.24811.
755
756 Pollitz, F. F., C. Wicks,,and W. Thatcher (2001), Mantle flow beneath a continental
757 strike-slip fault: Postseismic deformation after the 1999 Hector Mine earthquake,
758 *Science*, 293(5536), 1814-1818, doi: 10.1126/science.1061361.
759
760 Pollitz, F., W.H. Bakun, and M. Nyst (2004), A physical model for strain accumulation in
761 the San Francisco Bay region: Stress evolution since 1838, *J. Geophys. Res.*, 109(B11).

762

763 Rolandone, F., R. Bürgmann, D. C. Agnew, I. A. Johanson, D. C. Templeton, M. A.
764 D’Alessio, S. J. Titus, C. Demets, and B. Tikoff (2008), Aseismic slip and fault-normal
765 strain along the central creeping section of the San Andreas fault, *Geophys. Res. Lett.*,
766 35(14), 10.1029/2008GL034437.

767

768 Savage, J. and W. Prescott (1978), Asthenosphere readjustment and the earthquake cycle,
769 *J. Geophys. Res.*, 83(B7), 3369–3376.

770

771 Savage, J. C. and M. Lisowski (1998), Viscoelastic coupling model of the San Andreas
772 fault along the big bend, southern California, *J. Geophys. Res.*, 103.B4, 7281-7292.

773

774 Schmalzle, G., T. Dixon, R. Malservisi, and R. Govers (2006), Strain accumulation
775 across the Carrizo segment of the San Andreas Fault, California: Impact of laterally
776 varying crustal properties, *J. Geophys. Res.*, 111(B5).

777

778 Shen, Z.-K., R. King, D. Agnew, M. Wang, T. Herring, D. Dong, and P. Fang (2011), A
779 unified analysis of crustal motion in southern California, 1970–2004: The SCEC crustal
780 motion map, *J. Geophys. Res.*, 116(B11).

781

782 Sieh, K., D.H. Natawidjaja, A.J. Meltzner, C. C. Shen, H.Cheng, K.S. Li, B.W.
783 Suwargadi, J. Galetzka, B. Philibosian and R.L. Edwards (2008). Earthquake supercycles
784 inferred from sea-level changes recorded in the corals of west Sumatra, *Science*,
785 322(5908), 1674-1678.

786

787 Smith, B. and D. Sandwell (2004), A three-dimensional semianalytic viscoelastic model
788 for time-dependent analyses of the earthquake cycle, *J. Geophys. Res.*, 109(B12),
789 doi:10.1029/2004JB003185.

790

791 Smith, B. and D. T. Sandwell (2006), A model of the earthquake cycle along the San
792 Andreas Fault system for the past 1000 years, *J. Geophys. Res.*, 111(B1),
793 10.1029/2005JB003703.

794

795 Smith-Konter, B. and D. Sandwell (2009), Stress evolution of the San Andreas Fault
796 System: Recurrence interval versus locking depth, *Geophysical Research Letters*,
797 36(L13304), doi:10.1029/2009GL037235.

798

799 Smith-Konter, B., D. T. Sandwell, and P. Shearer (2011), Locking depths estimated from
800 geodesy and seismology along the San Andreas Fault System: Implications for seismic
801 moment release, *J. Geophys. Res.*, 116(B6).

802

803 Solis, T., (2013) Estimating variations in locking depth for the Mojave segment of the
804 San Andreas fault over the past 1500 years from paleoseismic stress drop, M.S. Thesis,
805 Unveristy of Texas at El Paso, U.S.A.

806

807 Spinler J.C., R.A. Bennett, M.L. Anderson, S.F. McGill, S. Hreinsdottir, and A.
808 McCallister (2010), Present-day strain accumulation and slip rates associated with
809 southern San Andreas and Eastern California shear zone faults: *J. Geophys. Res.*, 115,
810 B11407, doi:10.1029/2010JB007424.

811
812 Titus, S. J., C. Demets, and B. Tikoff (2006), Thirty-five-year creep rates for the creeping
813 segment of the San Andreas Fault and the effects of the 2004 Parkfield earthquake:
814 Constraints from alignment arrays, continuous Global Positioning System, and
815 creepmeters, *Bulletin of the Seismological Society of America*, 96(4), S250–S268,
816 10.1785/0120050811.

817
818 Toké, N. A., J.R. Arrowsmith, M.J. Rymer, A. Landgraf, D.E. Haddad, M. Busch, J.
819 Coyan, and A. Hannah (2011), Late Holocene slip rate of the San Andreas fault and its
820 accommodation by creep and moderate-magnitude earthquakes at Parkfield, California
821 *Geology*, 39, p. 243-246, doi:10.1130/G31498.1.

822
823 Tong, X., D. Sandwell, and B. Smith-Konter (2012), A systematic estimation of fault
824 creep rates along major faults in California from L-band radar interferometry, paper
825 presented at Annual Meeting of Southern California Earthquake Center, Univ. Southern
826 California / Southern California Earthquake Center, Palm Springs, California, U.S.A.

827
828 Tong, X., D. Sandwell, and B. Smith-Konter (2013), High-resolution interseismic
829 velocity data along the San Andreas Fault from GPS and InSAR, *J. Geophys. Res. Solid*
830 *Earth*, 118, doi:10.1029/2012JB009442.

831
832 van der Woerd, J., Y. Klinger, K. Sieh, P. Tapponnier, F. J. Ryerson, and A.-S. Mériaux
833 (2006), Long-term slip rate of the southern San Andreas Fault from ¹⁰Be-²⁶Al surface
834 exposure dating of an offset alluvial fan, *J. Geophys. Res.*, 111, B04407,
835 doi:10.1029/2004JB003559.

836
837 Wang, R., F. L. Martin, and F. Roth (2003), Computation of deformation induced by
838 earthquakes in a multi-layered elastic crust—fortran programs edgrn/edcmp, *Computers*
839 *and Geosciences*, 29(2), 195–207.

840
841 Watts, A. B. (2007), Crust and lithosphere dynamics: An overview, in *Treatise on*
842 *Geophysics*, edited by Gerald Schubert, pages 1 – 48., Elsevier, Amsterdam, 2007.

843
844 Wdowinski, S., B. Smith-Konter, Y. Bock, and D. Sandwell (2007), Diffuse interseismic
845 deformation across the Pacific–North America plate boundary, *Geology*, 35(4), 311–314.

846
847 Zeng, Y., and Z.-K. Shen (2010), A kinematic fault network model of crustal deformation
848 for California and its application to the seismic hazard analysis, Tech. rep., U.S.
849 Geological Survey, Golden, Colo., U.S.A.

850
851
852

853
854
855
856
857
858
859

860 **Acknowledgement**

861

862 This work was supported by NSF grant EAR-1147427 (EarthScope) and EAR-0847499.

863 We are grateful to Dr. Tom Herring, Dr. Yuehua Zeng, Dr. ZhengKang Shen for useful
864 discussions and suggestions.

1 **Figure captions**

2

3 **Figure 1.** A regional topography map of the San Andreas Fault System in California
4 shown in an Oblique Mercator projection. The black line segments represents the fault
5 segments studied in this paper. Each fault segment is labeled by a 3-characters name
6 (Table 1). The white stars represent three major earthquakes that are believed to cause
7 significant postseismic relaxation in the lower crust and upper mantle.

8

9 **Figure 2.** 1989 GPS (triangles) velocity vectors and 53,792 InSAR LOS velocity data
10 points (colored grid) along the SAFS in California, shown in an Oblique Mercator
11 projection. The projection pole (-74.4° W, 50.1° N) is from *Wdowinski et al.* [2007]. The
12 InSAR data spans 4.5 years (2006.5-2010) and are derived from 1100 ALOS radar
13 interferograms. The radar flight direction (ascending) and look direction are provided.
14 Positive velocities (red) represent ground motion away from the satellite. The geological
15 fault traces are shown as black lines. The thin black lines with alphabet letters
16 corresponds to the profiles shown in Figure 7A and 7B.

17

18 **Figure 3.** Comparison between our earthquake cycle model (solid lines) and 2D analytic
19 models (dash lines). The cross-sections of the fault parallel velocity at surface were
20 shown. We considered a 60 km thick plate with an effective viscosity of approximately
21 10^{19} Pa s in this comparison. The fault slips at plate rate from the locking depth (15 km)
22 to the bottom of the elastic plate. We prescribed 20 earthquakes with recurrence interval
23 of 100 years. The time is normalized by the Maxwell time (20 years). The colored lines
24 represent different time periods during the earthquake cycle. It is clear that the numerical
25 model accurately reproduces the analytical solution at different times within an
26 earthquake cycle.

27

28 **Figure 4.** Grid-search to determine the relative weighting factors used in the inversion. a)
29 weight for the C-matrix; b) weight for GPS; c) weight for InSAR. The triangles are the
30 weighted RMS misfit to the GPS data and the circles are the weighted RMS misfit to the
31 InSAR data. The actual weights used in the slip rate inversion is 0.3 for GPS, 0.2 for
32 InSAR and 0.1 for the geological constrain.

33

34 **Figure 5.** The fit to the GPS data. In the top figure a) the black arrows show the observed
35 GPS horizontal velocity vectors with 95% confidence interval. The blue arrows show the
36 predicted horizontal velocity vectors from the preferred plate model PL6019. The bottom
37 figure b) shows the GPS residual (observation - model) velocity vectors. Note the
38 different scales used in the two figures. The thin gray curves denote the fault segments.

39

40 **Figure 6.** The fit to the InSAR LOS velocity data. Positive velocities (red) represent
41 ground motion away from the satellite. The radar look direction and flight direction is
42 marked in Figure 2. a) Observed InSAR LOS velocity. b) Predicted InSAR LOS velocity
43 from the preferred plate model PL6019. c) Residuals (observation - model) of the InSAR
44 LOS velocity. The thin black curves denote the fault segments.

45

46 **Figure 7A.** Cross-sections showing the GPS velocity data and its fit to the deformation
47 models. The GPS velocity vectors are decomposed into two components (parallel and
48 perpendicular to the plate motion) using an Euler pole (-74.4° W, 50.1° N). The
49 parallel components are shown as triangles, compared to the modeled velocity (solid
50 line). The profiles are all running in $N45^{\circ}E$. The profile is labeled by alphabet letter in the
51 upper right of each subfigure (Figure 2). The geographic region of the profile is named at
52 the top of each subfigure. Three models are considered here: HS model (black line),
53 PL6019 model (blue line), and PL3019 model (red line). The RMS misfit of each profile
54 to the models are shown in the following order HS/PL6019/PL3019. The locations of the
55 major faults are marked by black diamonds at the bottom of each subfigure with
56 explanations below: BSZ-Brawley seismic zone, SAF-San Andreas fault, SJF-San Jacinto
57 fault, HAY-Hayward fault, MAA-Maacama fault, ROD-Rodgers Creek fault. The left
58 side of the subfigure is the west side of the profiles. The error bar of the GPS data show
59 one standard deviation. Inside profile g, we tested a dipping fault model shown as dashed
60 black lines. See text for details.

61

62 **Figure 7B.** Continuation of Figure 7A.

63

64 **Figure 8.** a) Geodetic slip rates in comparison to the geological slip rates. Geodetic slip
65 rates are from HS model. The 3-character labels for fast slipping fault segments (slip
66 rates > 10 mm/yr) are shown (Figure 1, Table 1). The horizontal error bars represent the
67 upper and lower bounds of the geological estimates, the vertical error bars represent the
68 uncertainties estimated in the slip rate inversion. The overall RMS misfits to the GPS,
69 InSAR, and preferred geological slip rates are shown in the upper left. b) Geodetic slip
70 rates are from PL6019 model. c) Geodetic slip rates are from PL3019 model. d) Geodetic
71 slip rates are from PL3020 model.

72

Table 1. Summary of the fault segments, locking depths, past earthquakes, geologic and geodetic fault slip rates of the SAFS.

Fault label	Fault name	Recurrence interval (years)	Date of the historical earthquakes	Locking depth (km)	Preferred geologic slip rate (mm/yr)	Bounds on the geological slip rates (mm/yr)	Geodetic slip rate from HS model (mm/yr)	Uncertainties of the geodetic slip rate from HS model (mm/yr)	Geodetic slip rate from PL6019 model (mm/yr)	Uncertainties of the geodetic slip rate from PL6019 model (mm/yr)	Geodetic slip rate from PL3019 model (mm/yr)	Uncertainties of the geodetic slip rate from PL3019 model	Geodetic slip rates from PL3020 model (mm/yr)	uncertainties of the geodetic slip rates from PL3020 model (mm/yr)
-------------	------------	-----------------------------	------------------------------------	--------------------	--------------------------------------	---	--	---	--	---	--	---	---	--

												(mm/yr)		
CER	Cerro_Prieto	200	1825 1915 1927 1934 1966	10.0	35	30 ~ 40	42.1	0.8	41.7	0.8	37.1	0.7	39.5	0.8
IMP	Imperial	200	1525 1575 1650 1700 1875 1915 1940 1979	5.9	35	15 ~ 40	44.1	1.0	44.0	1.0	43.0	1.0	43.9	1.0
BSZ	Brawley	200	1700 1875 1906 1979	12.0	25	15 ~ 30	23.5	0.5	24.6	0.5	32.7	0.5	30.7	0.5
COA	Coachella	200	774 824 982 1020 1107 1230 1300 1347 1475 1503 1683	11.5	20	15 ~ 30	19.7	0.5	19.5	0.5	19.6	0.6	22.8	0.5
SSB	South_San_Bernardino	200	774 824 982 1020 1107 1230 1300 1347 1475 1503 1683 1987	16.4	13	5 ~ 20	17.4	0.2	21.1	0.5	25.5	0.7	19.2	0.4

NSB	North_Sa n_Bernard ino	200	774 931 1173 1107 1313 1347 1450 1475 1500 1619 1684 1704	17.8	19	13 ~ 28	16.0	0.4	15.2	0.4	13.5	0.5	14.1	0.5
SUP	Superstiti on_Hills and Superstiti on Mount combined	600	1050 1460 1540 1987	10.8	11	4 ~ 15	11.4	0.5	16.7	0.6	13.2	0.6	13.9	0.6
BOR	Borrogo_ Mountain	550	1050 1460 1540 1987	10.0	5	1 ~ 10	7.1	0.3	10.8	0.3	14.3	0.3	9.1	0.3
COY	Coyote_C reek	500	1892 1968	10.0	5	1 ~ 10	8.9	0.4	10.6	0.4	11.9	0.4	8.8	0.4
ANZ	Anza	300	1892 1942 1954 1968 1969 1987	10.0	14	11 ~ 18	15.1	0.3	16.4	0.3	16.9	0.4	14.7	0.3
CLA	Clark	300	1020 1230 1290 1360 1630 1760	12.0	8	6 ~ 11	10.1	0.4	9.7	0.4	8.7	0.4	8.9	0.5
SJV	SJ_Valley	450	1770 1899 1918	15.0	16	12 ~ 24	15.1	0.5	15.9	0.5	17.8	0.4	16.4	0.4
SJB	SJ_San Bernadino valley	500	1770 1923	15.0	6	2 ~ 8	4.6	0.5	5.9	0.5	12.4	0.6	7.8	0.6

MOJ	Mojave	220	533 634 697 722 781 850 1016 1116 1264 1360 1487 1536 1685 1812 1857	15.0	34	25 ~ 40	25.5	0.3	27.8	0.3	33.1	0.4	22.9	0.3
SCZ	S_Carrizo (big bend)	250	599 1078 1247 1277 1310 1384 1393 1417 1457 1462 1565 1571 1614 1713 1749 1857	15.0	34	31 ~ 37	36.2	0.3	36.3	0.3	36.9	0.3	31.7	0.3

CAZ	Carrizo	200	599 1078 1247 1277 1310 1384 1393 1417 1457 1462 1565 1571 1614 1713 1749 1857	15.0	34	31 ~ 37	36.2	0.3	36.3	0.3	37.2	0.3	33.1	0.3
CHO	Cholame	200	1857	12.0	34	29 ~ 39	32.2	0.2	33.0	0.2	34.5	0.2	32.4	0.2
PAR	Parkfield	20	1857 1881 1901 1922 1934 1966	12.0	34	26 ~ 39	34.0	0.5	34.9	0.5	37.7	0.5	35.0	0.5
CRE	Creeping	250	N/A	12.0	34	29 ~ 39	34.5	0.3	38.7	0.4	43.8	0.4	36.3	0.4
SCR	Santa_Cruz_Mt	150	1300 1600 1838 1890 1906 1989	12.0	17	13 ~ 21	15.7	0.5	17.1	0.5	19.7	0.5	17.2	0.5
PEN	SA_Peninsula	230	1300 1600 1838 1906	16.2	17	13 ~ 21	18.1	0.4	20.5	0.4	25.4	0.4	17.6	0.4
SNC	S_SA_N_Coast	230	1300 1600 1906	15.5	24	16 ~ 27	14.0	0.4	23.0	0.5	36.5	0.7	33.2	0.6
NNC	N_SA_N_Coast	270	1300 1600 1899 1906	13.2	24	16 ~ 27	19.0	0.7	22.2	0.9	21.3	1.0	20.0	0.9

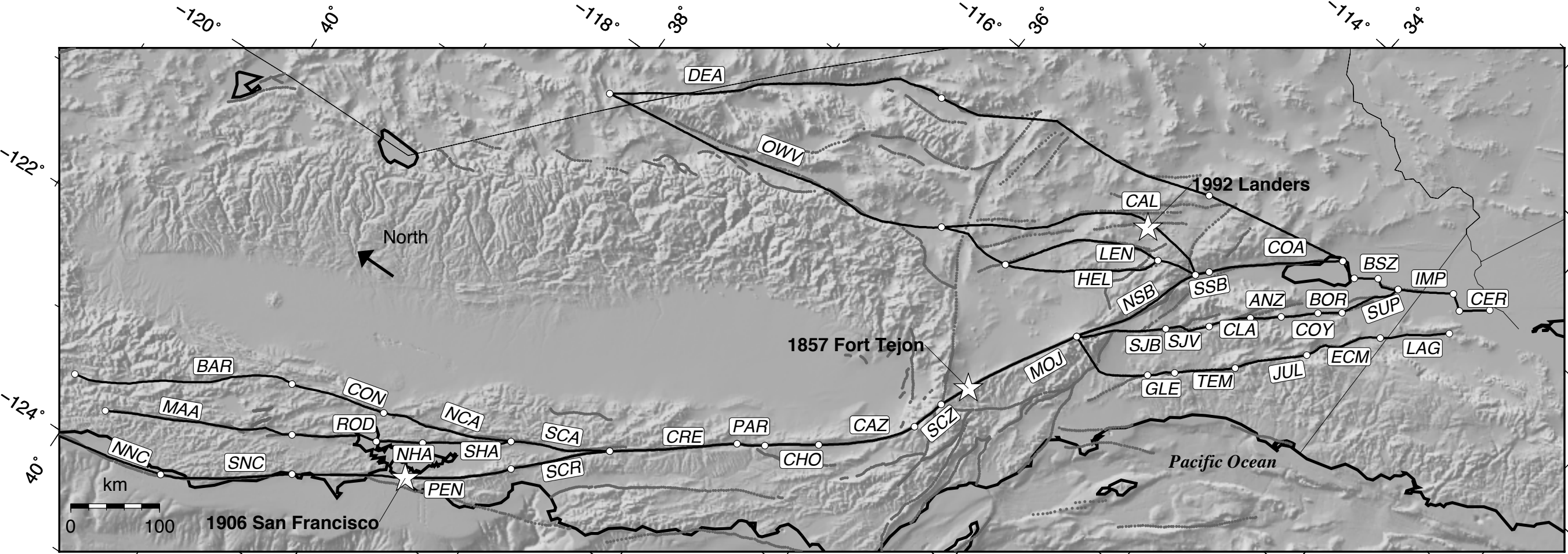
SCA	S._Calaveras	300	1864 1897 1911 1984	12.0	15	10 ~ 20	16.1	0.3	19.5	0.3	21.0	0.4	19.0	0.3
NCA	N._Calaveras	550	1864	12.0	6	3 ~ 8	9.0	0.3	10.4	0.4	10.0	0.5	9.0	0.4
CON	Concord	3000	510	12.0	4.3	3 ~ 9	7.7	0.5	9.0	0.5	10.7	0.5	9.1	0.5
BAR	Hunting Creek/Bar lett Spring	500	1760	12.0	4	2 ~ 9	7.3	0.4	8.5	0.4	8.5	0.5	10.1	0.4
SHA	S._Hayward	200	1470 1630 1730 1868	12.0	9	7 ~ 11	9.2	0.1	9.5	0.1	11.2	0.1	9.7	0.1
NHA	N._Hayward	300	1708	12.0	9	7 ~ 11	9.8	0.1	9.8	0.1	10.4	0.1	9.7	0.1
ROD	Rodgers_ Creek	400	1898	12.0	9	6 ~ 11	12.0	0.2	12.0	0.3	12.6	0.3	10.2	0.3
MAA	Maacama	250	N/A	12.0	9	6 ~ 12	9.8	0.3	10.8	0.3	15.1	0.3	12.7	0.3
LAG	Laguna_S alada	1000	1892	9.0	3	1 ~ 5	2.9	0.2	5.4	0.2	7.2	0.3	5.4	0.2
GLE	Elsinore_ GlenIvy	1000	963 1230 1283 1440 1627 1850 1910	10.0	5	3 ~ 7	4.7	0.1	4.7	0.1	4.6	0.1	4.6	0.1
TEM	Elsinore_ Temecula	1000	1655 1810	10.0	5	3 ~ 7	4.0	0.2	4.0	0.2	3.2	0.2	3.6	0.1
JUL	Elsinore_J ulian	1500	1655 1680 1753 1804	10.0	3	1 ~ 5	0.0	0.0	0.0	0.0	0.0	0.0	0.0	0.0
ECM	Elsinore_ Coyote_ Mt	1500	1650 1892	10.0	3	1 ~ 5	2.1	0.3	1.2	0.3	0.4	0.3	5.5	0.4
LEN	Lenwood - Lockhart - Old Woman Springs	3000	1100	12.0	1	0.6 ~ 1.4	3.9	0.6	4.2	0.7	2.9	0.8	6.0	0.6
HEL	Helendale	3000	1100	12.0	0.6	0.2 ~ 1.0	0.4	0.4	0.8	0.5	1.1	0.6	0.0	0.0
CAL	Calico- Hidalgo	3000	510	10.0	1.6	1.0 ~ 2.8	6.9	0.3	7.3	0.3	7.7	0.3	6.6	0.4
OWV	Owens_V alley	3000	1100 1872	11.5	3.5	2 ~ 5	7.1	0.1	6.2	0.1	4.0	0.1	4.6	0.1
DEA	Death_Va lley	1000	1100	12.0	3	2 ~ 4	5.0	0.3	5.0	0.3	6.5	0.3	5.7	0.3

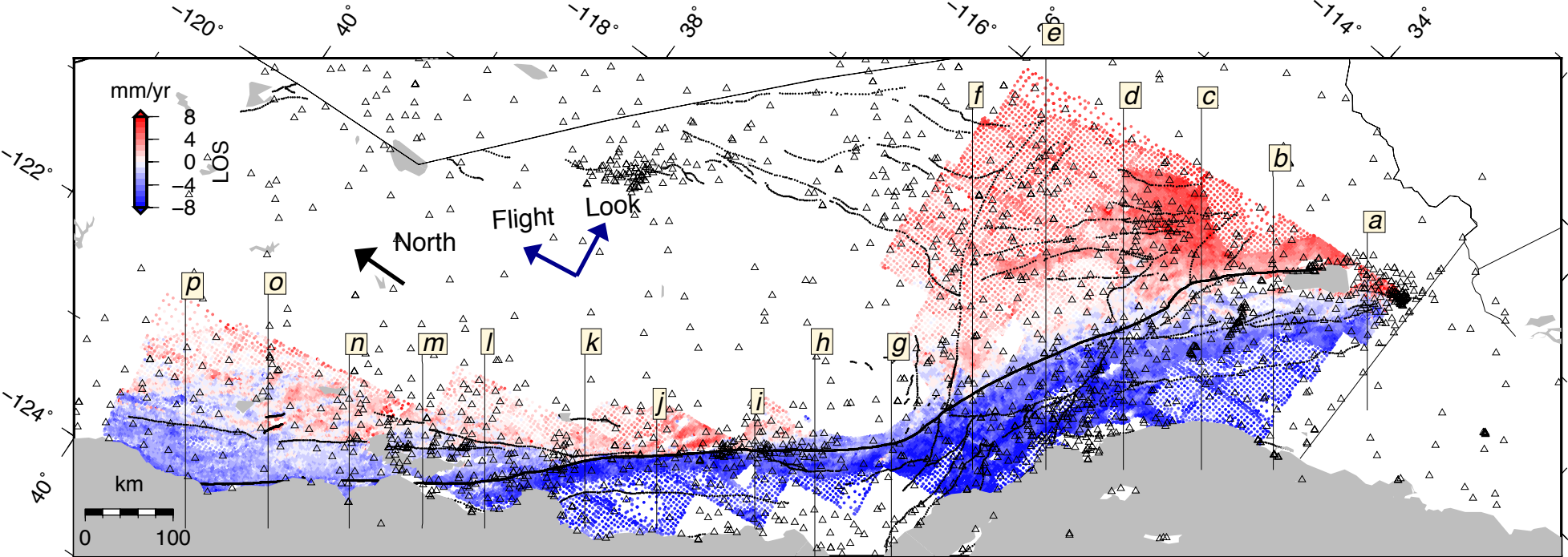
Table 2. Fit to GPS, InSAR and geologic data for four different rheological models.

Model	HS	PL6019	PL3019	PL3020
GPS χ^2 misfit	2.67	2.56	2.74	2.68
GPS WRMS (mm/yr)	1.71	1.68	1.73	1.72
InSAR χ^2 misfit	0.28	0.27	0.27	0.28
InSAR WRMS (mm/yr)	1.34	1.30	1.31	1.34
RMS to the preferred geology slip rate (mm/yr)	3.50	3.70	5.30	4.00

Table 3. Summary of the synthetic test on the 1857 Fort Tejon earthquake.

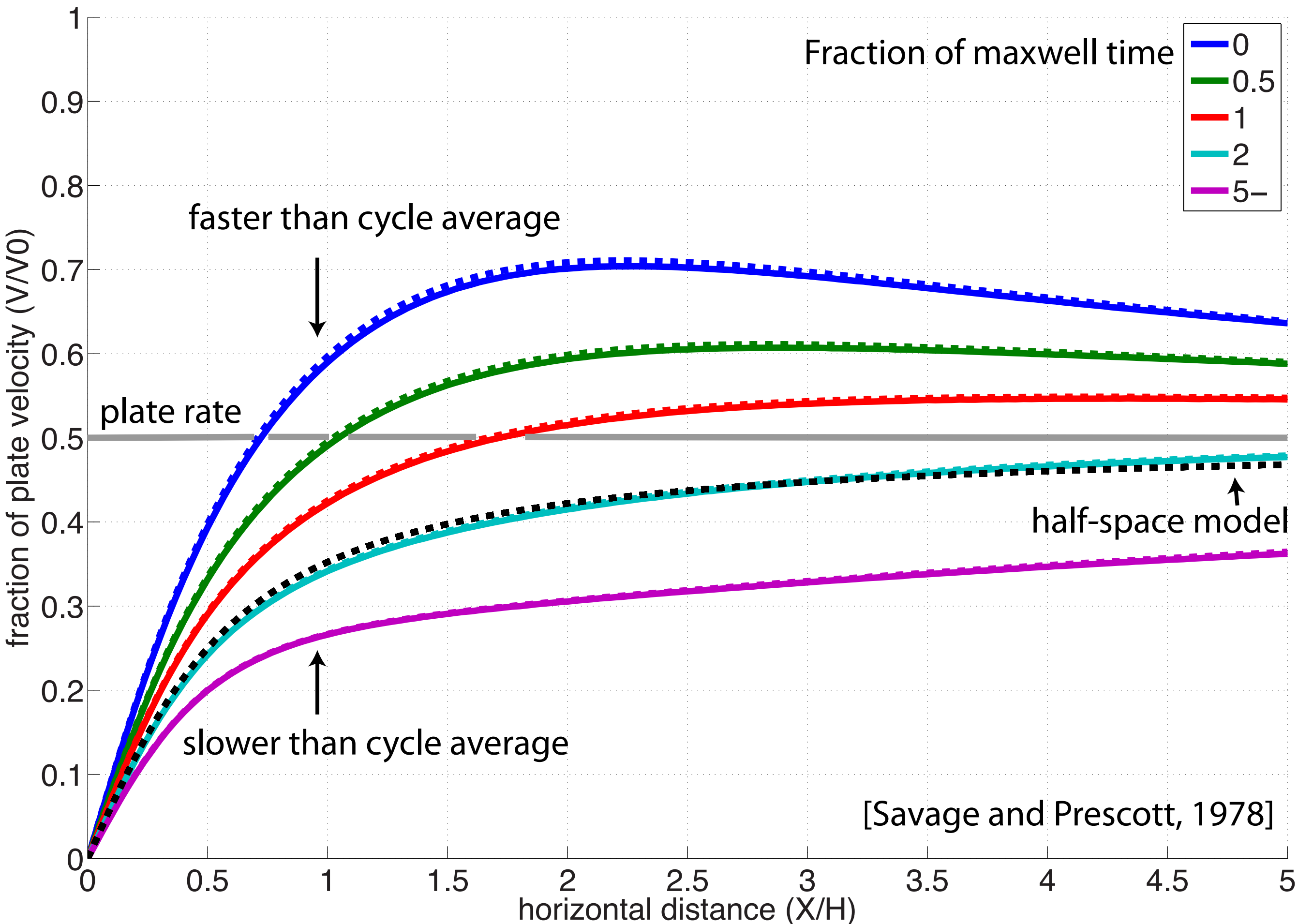
Mojave segment slip rate (mm/yr)	scenario A	scenario B	scenario C	no change
PL6019	27.5	27.8	26.4	27.8
PL3019	32.5	33	28.4	33
PL3020	20.8	23.6	20.8	22.9

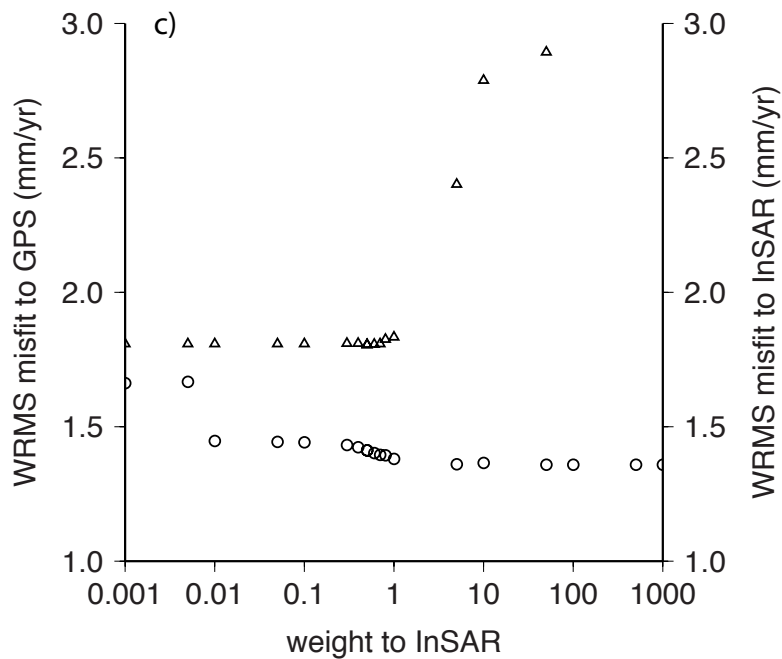
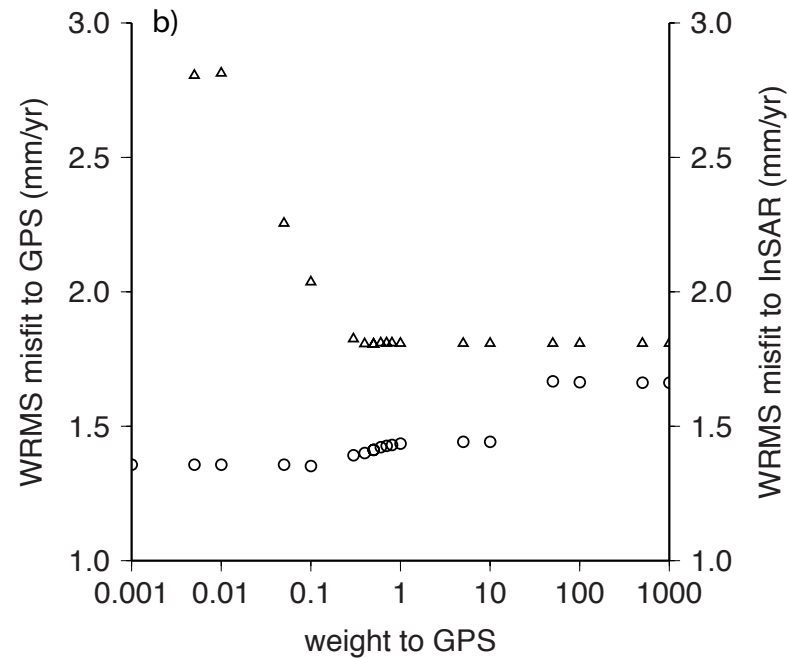
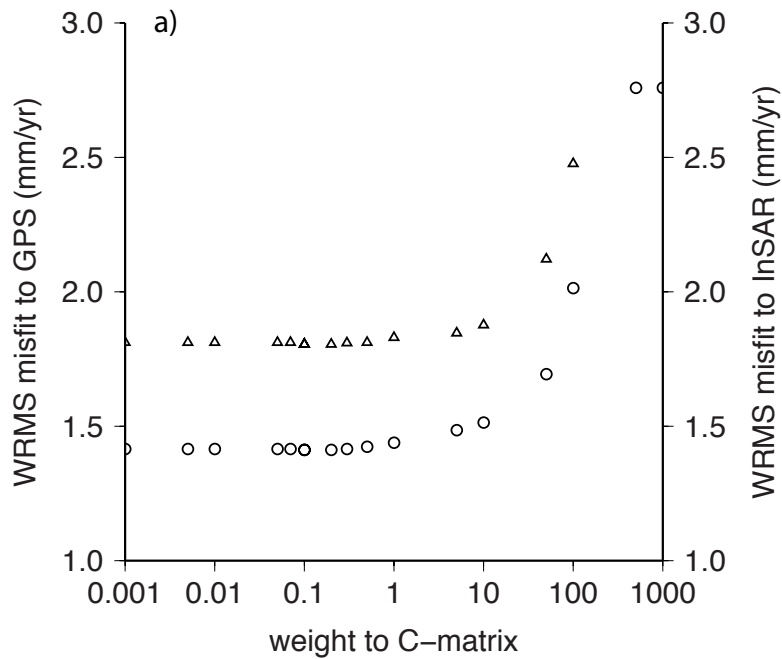


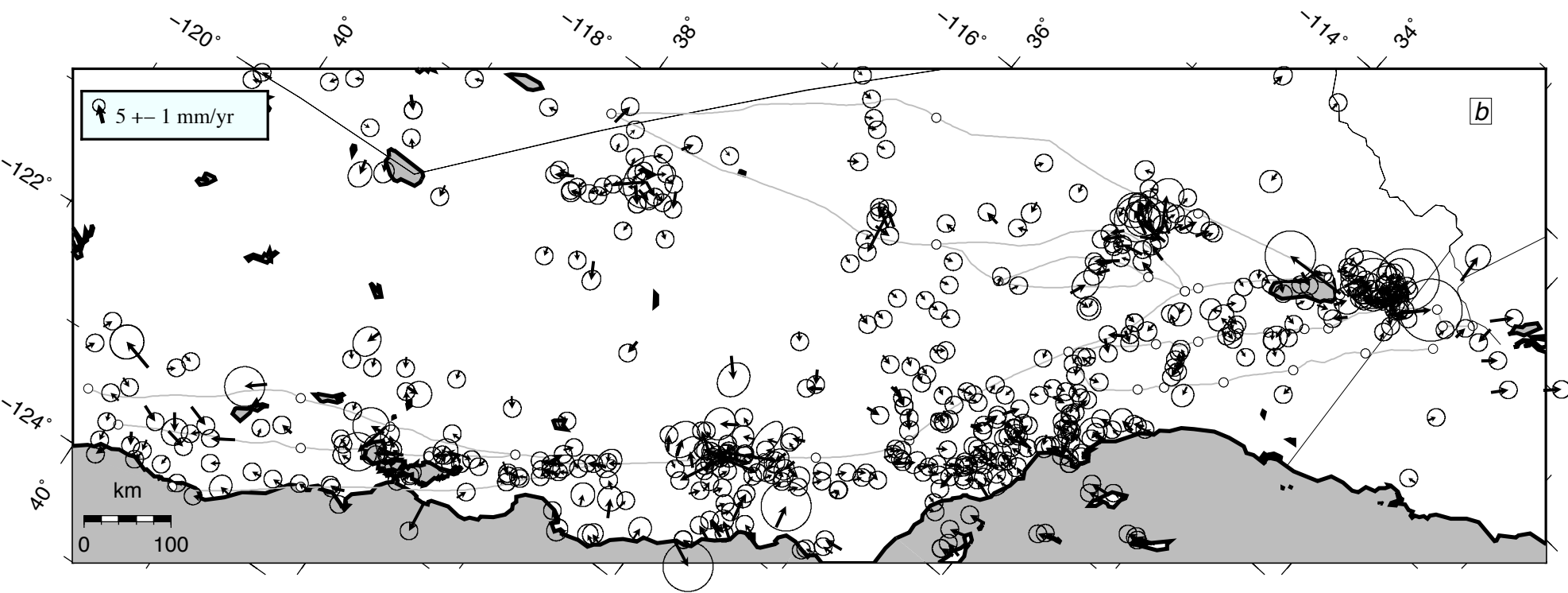
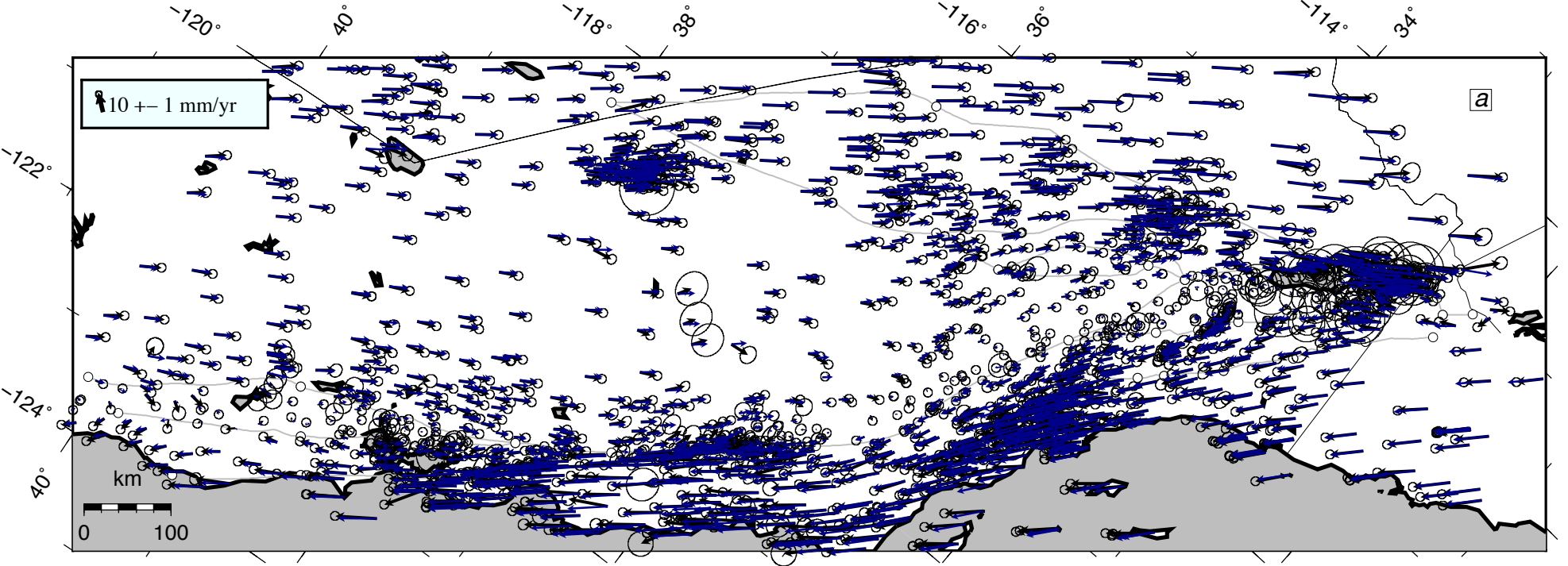


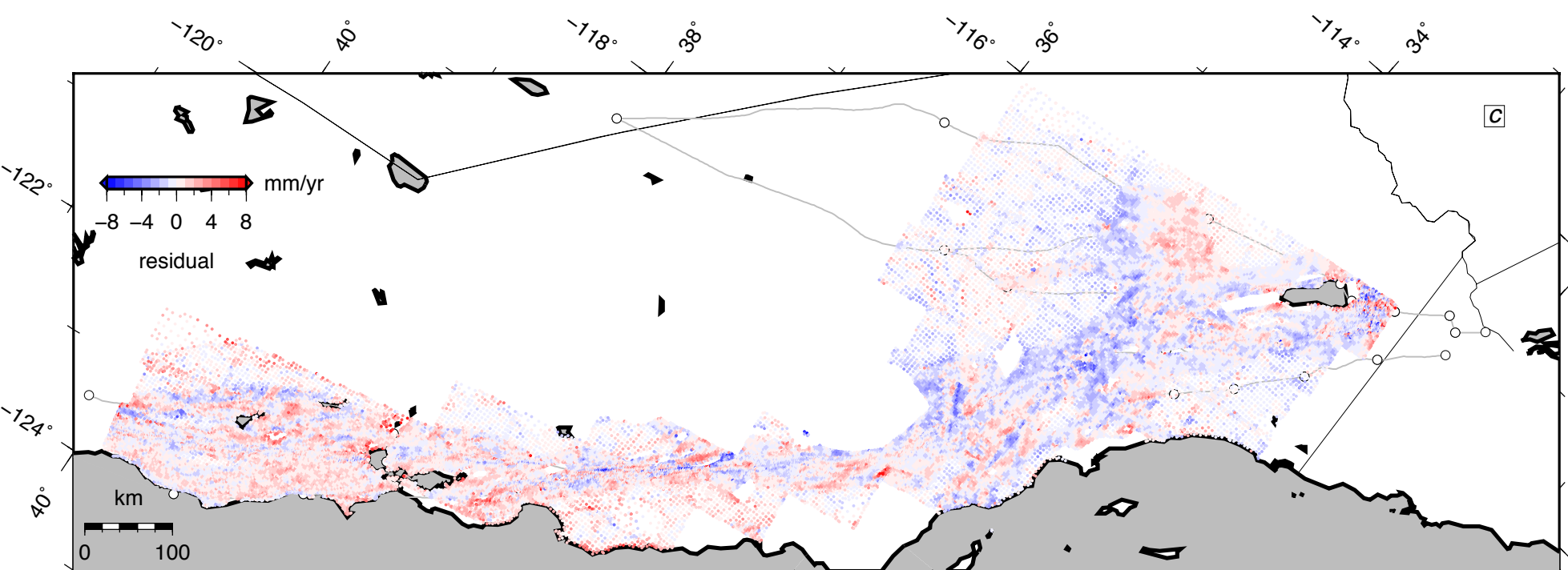
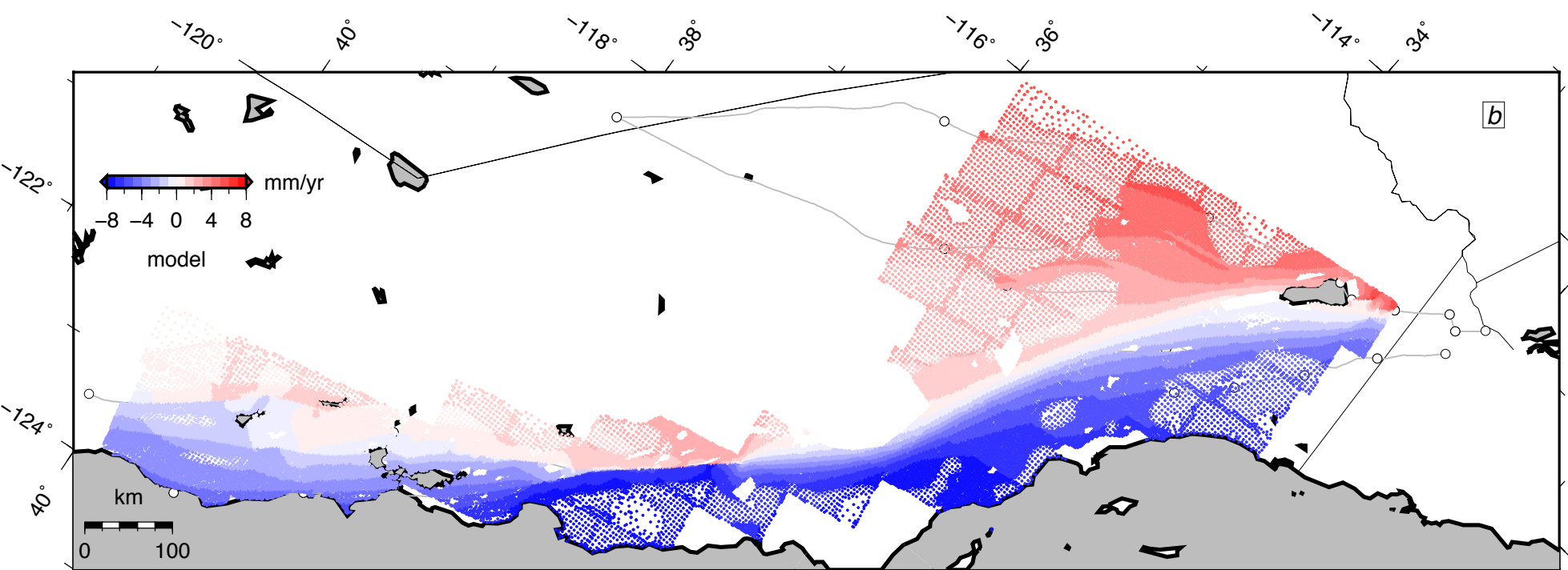
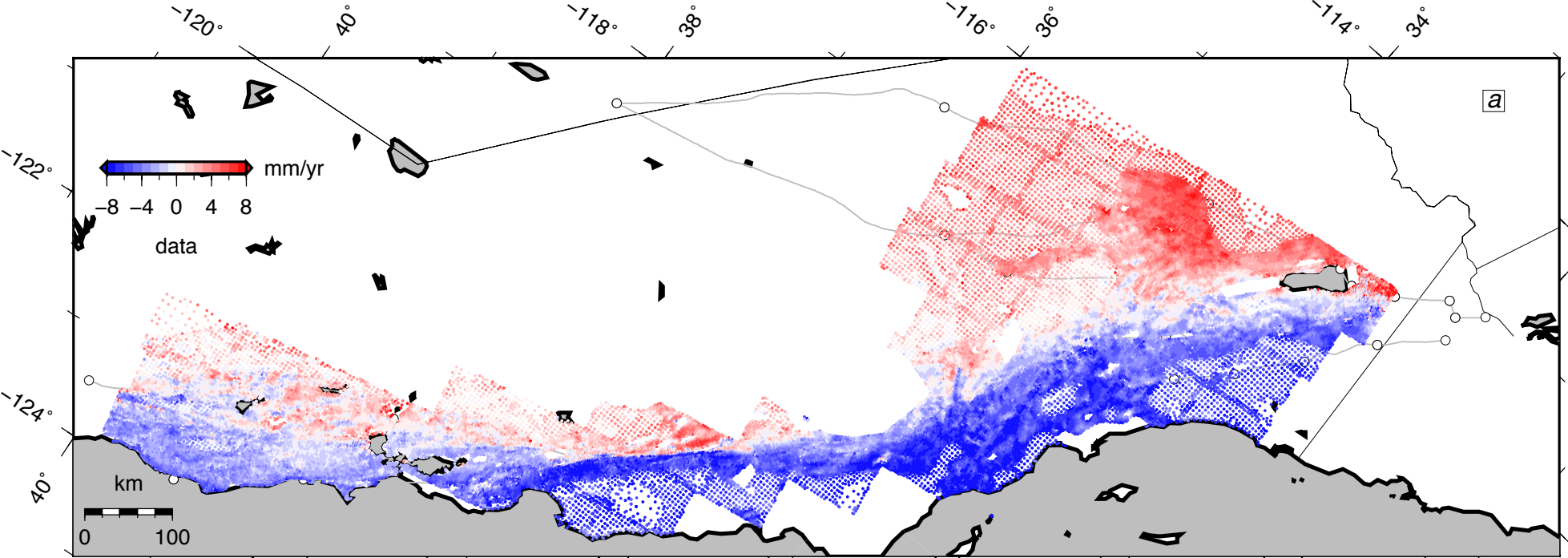
Earthquake cycle model (solid lines)
compared to analytic solution (dashed lines)

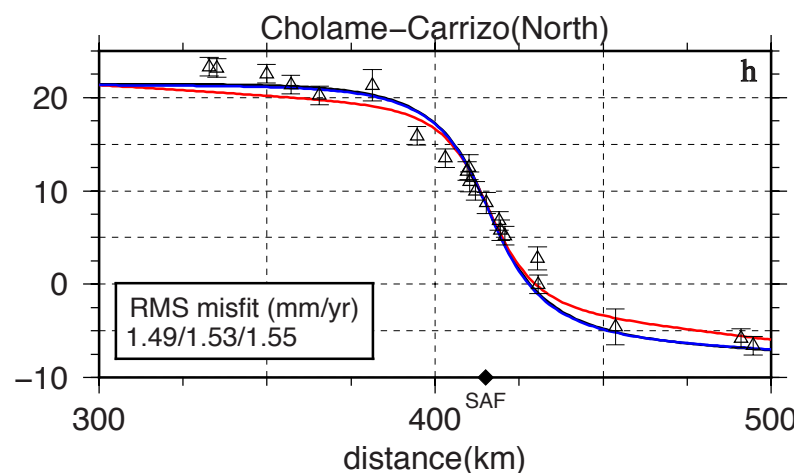
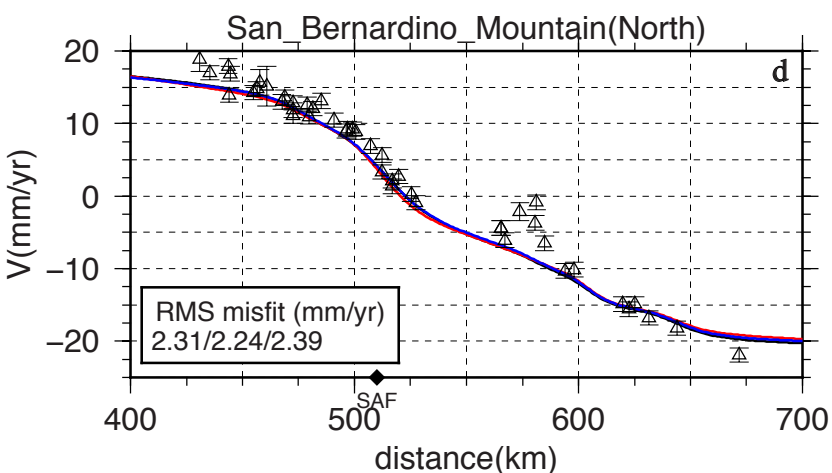
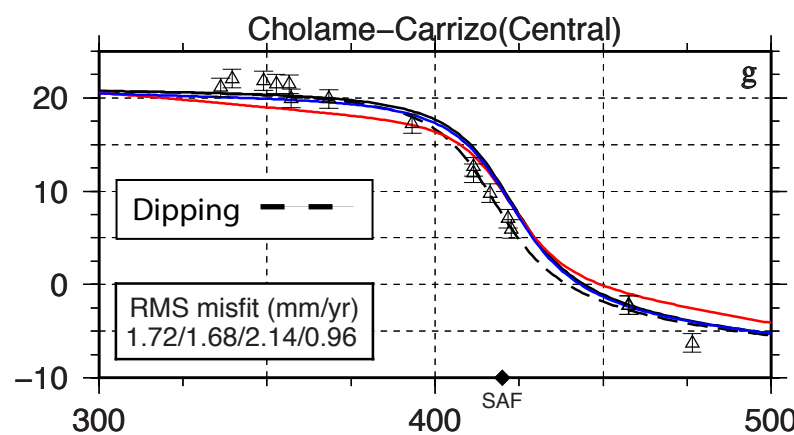
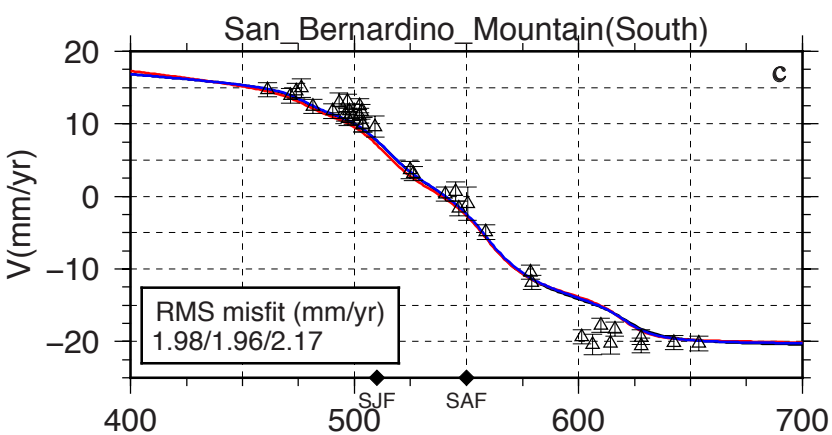
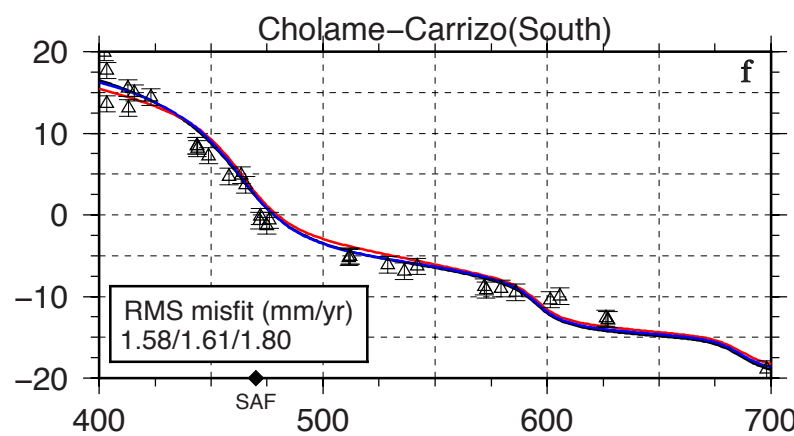
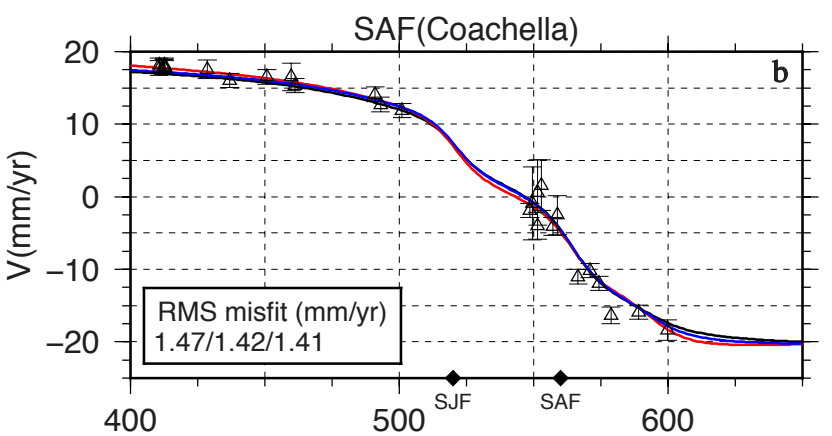
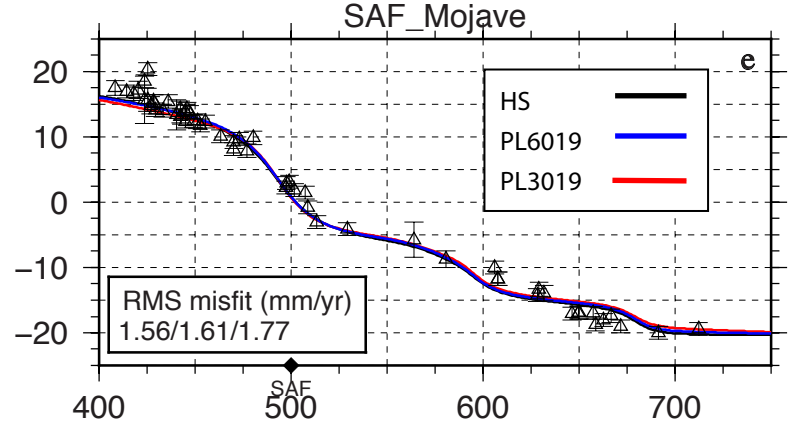
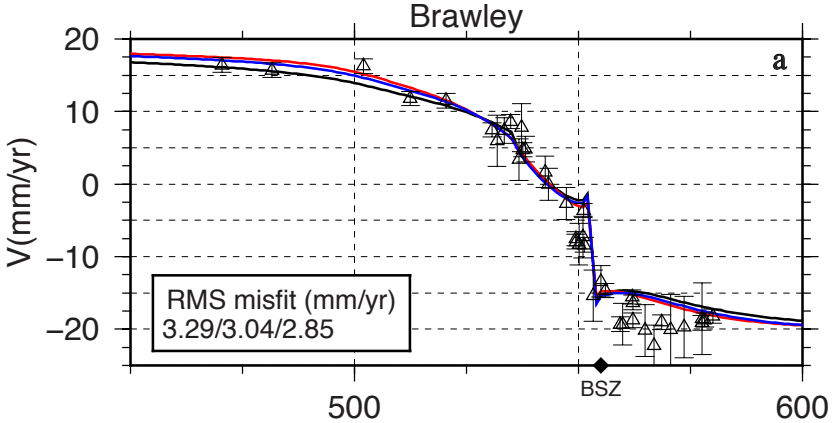
Maxwell time = 20 years

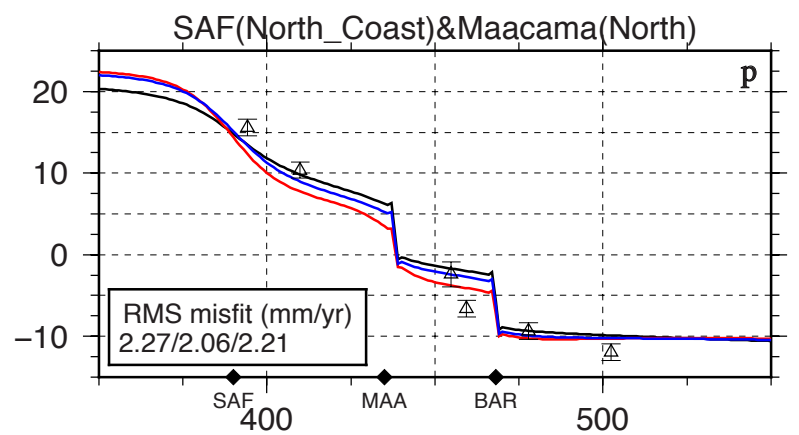
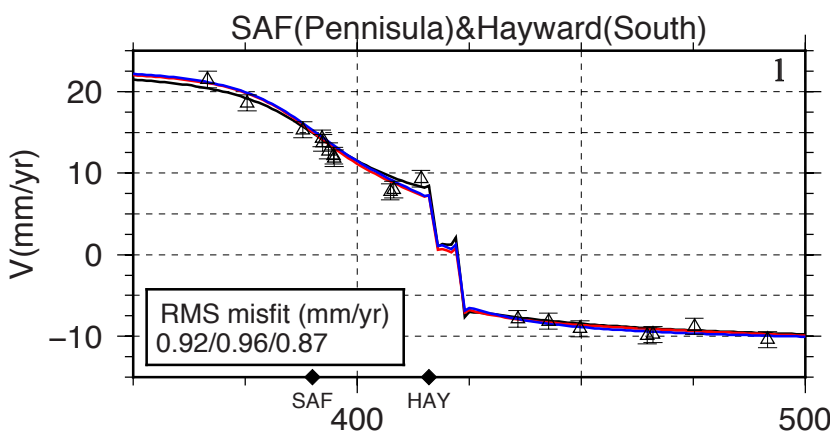
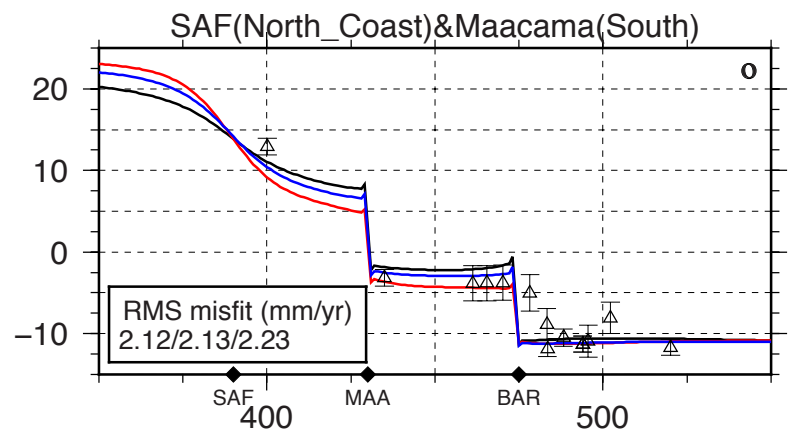
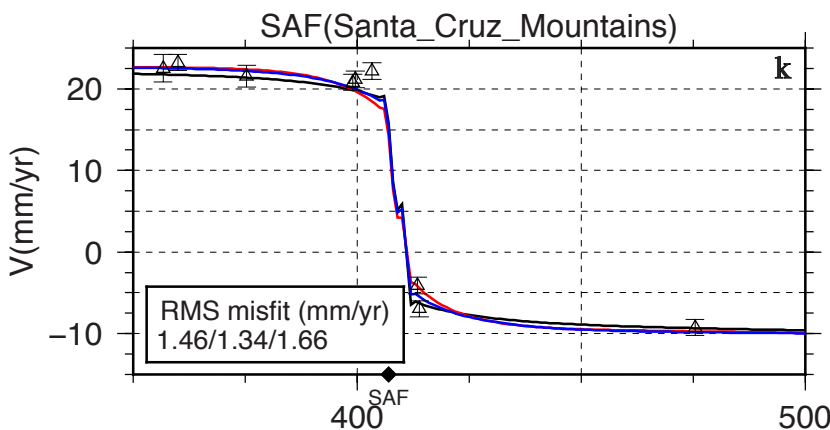
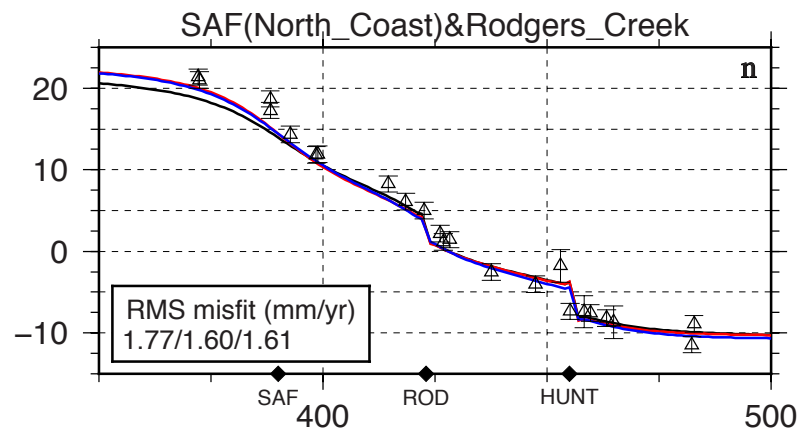
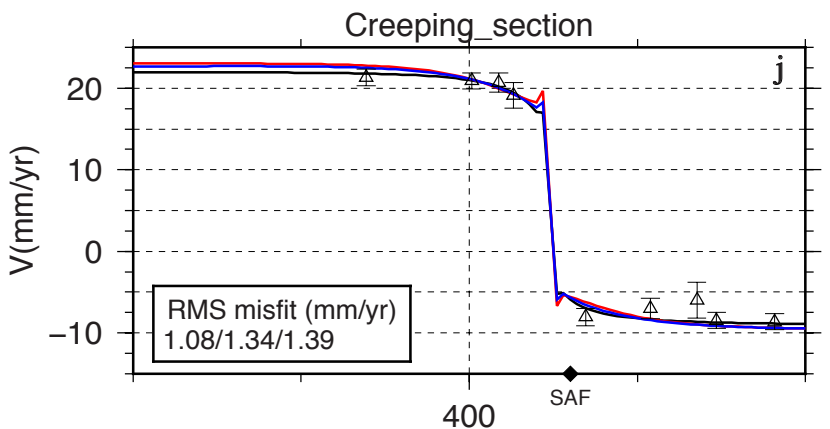
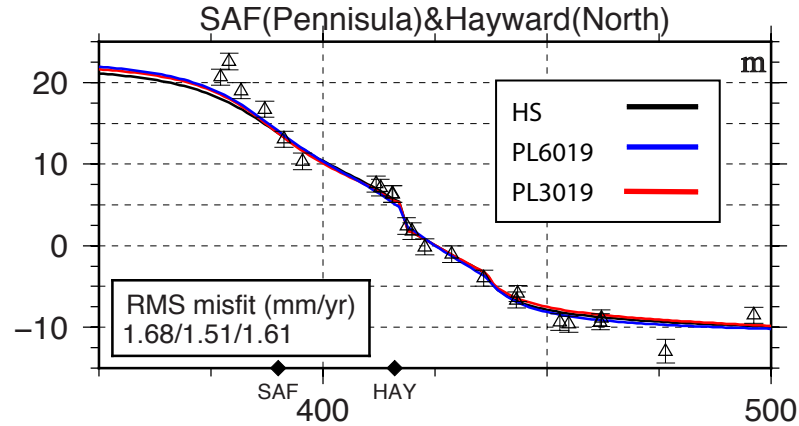
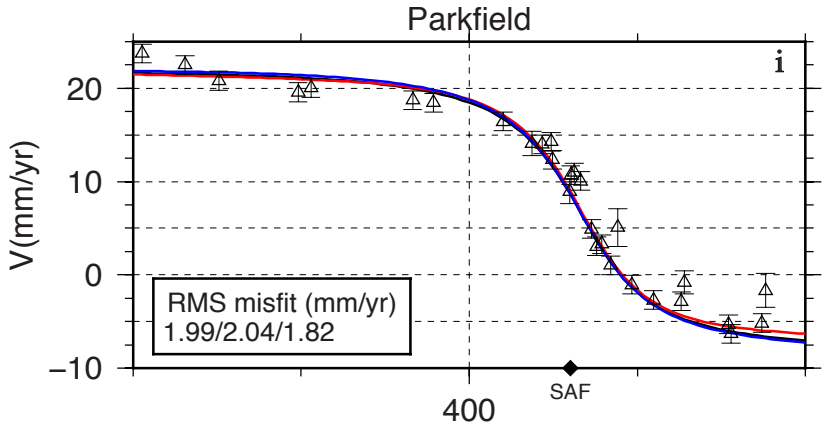












distance(km)

distance(km)

